UNIVERSITY OF RIJEKA

DEPARTMENT OF PHYSICS

Ivana Batković

STUDY OF AXION-LIKE PARTICLES SIGNATURES IN THE VERY-HIGH-ENERGY GAMMA-RAY SPECTRA OF ACTIVE GALACTIC NUCLEI

Master thesis

Rijeka, September 2020

UNIVERSITY OF RIJEKA
DEPARTMENT OF PHYSICS
ASTROPHYSICS AND ELEMENTARY PARTICLE PHYSICS

Master thesis

Study of axion-like particles signatures in the very-high-energy gamma-ray spectra of Active Galactic Nuclei

Supervisors:
dr. sc. Marina Manganaro
dr. sc. Gabrijela Zaharijaš

Candidate:
Ivana Batković

Rijeka, 21st September 2020

Contents

Abstract

The aim of this work of thesis is the investigation of axion-like particles (ALPs) signatures in the spectra of Active Galactic Nuclei (AGN), in the very-high-energy (VHE, E $>$ 100GeV) γ-ray range. ALPs, which are candidates for Dark Matter, in the presence of strong magnetic fields could interact with the γ rays emitted by AGNs, and this effect could be observed in the VHE γ-ray spectra under the form of "wiggles" or oscillations.
Here, the search for ALPs was performed on MAGIC (Major Atmospheric Gamma-ray Imaging Cherenkov) data of the AGN NGC 1275, located in the Perseus cluster. 54.1 hours of MAGIC data have been analysed. The conversion probability of γ rays in ALPs ($P_{\gamma\gamma}$) has been calculated for several values of the mass of ALPS (m_a) and coupling ($g_{a\gamma\gamma}$). A study of the parameter space for those two quantities has been performed.
We found three different states of the source which correspond to flaring, high and low activity state, respectively. Data from the flaring state were used for the search of ALPs signatures. The spectrum is stable in time in the energy range 50 GeV - 700 GeV, with an integral flux of $(8.5 \pm 0.2) \times 10^{-10}$ cm^{-2} s^{-1} above 100 GeV. The spectrum can be described by a power-law with an exponential cut-off (EPWL) with Γ index -2.4. In the study of ALPs parameters space, parameters combinations are narrowed down to 10 sets each with several possibilities of m_a and coupling $g_{a\gamma\gamma}$. Those sets are named S1 - S10 and the corresponding values of m_a and $g_{a\gamma\gamma}$ are in the ranges 90 neV - 110 neV and 0.3×10^{-11} GeV^{-1} - 0.5×10^{-11} GeV^{-1}, respectively. Using each set separately, the convolution of $P_{\gamma\gamma}$ with the EPWL fit was calculated and compared with the spectral energy distribution (SED) of the source. A quantitative preliminary comparison between the convolution and the intrinsic SED was performed by obtaining the sums of squared residuals for the dataset S1 - S10. We conclude that S10 (sum of squared residuals = 55.3), among the 10 sets studied, is the most promising set of parameters for the search of ALPs found in this preliminary study.

Keywords: galaxies: active – galaxies : individual : NGC 1275 – gamma-rays – axion-like particles – dark matter

1 Introduction

This work of thesis is focused on the quest for axion-like particles (ALPs) using the data taken by the MAGIC (Major Atmospheric Gamma-ray Imaging Cherenkov) telescopes, in the very-high-energy (VHE, E>100 GeV) γ-ray range. Axions arise as pseudo Nambu-Goldstone bosons associated to the breaking of the U(1) symmetry, proposed by Peccei and Quinn [1]. They constitute a solution to the strong CP problem. One of the results of this symmetry breaking is axion coupling to the electromagnetic field through the two-photon vertex. This anomalous coupling is investigated in various experimental searches for axions and ALPs (in e.g. [2, 3, 4, 5]). ALPs are a more general case of axions in which the two most important parameters, mass and their coupling to photons, are not mutually dependent. This characteristic makes their study model-independent. Axions and ALPs are intriguing particles also because they are among candidates that could explain the particle nature of dark matter [6] that is known to constitute 25% of the energy density of the Universe today. The theory of axions and ALPs which is related to this study, will be presented in Sec. 2.1.
Among the many searches done on the basis of photon-ALP interaction, some are performed in ground based laboratories with the goal of detecting ALPs in a resonant microwave cavity [3]. Some experiments are focused on detecting solar ALPs, coming from the Sun. They are known as helioscopes and probably the best known is the CERN Axion Solar Telescope (CAST) [1]. Depending on the type of the instrument and different experimental setup, different magnetic field and domain length are used. In laboratory experiments the parameter space that could be probed is restricted to masses of ALPs of the order of the μeV. Other than in the laboratory experiments, axions and ALPs can be studied in the astrophysics domain as well. Since the Universe is a "pool" of strong magnetic fields, spread over great distances, one can explore the possibility of photon-ALP conversion on their way to Earth from bright sources, such as supernovae or active galactic nuclei (AGN). Experiments conducted so far placed certain constraints on the ALPs parameter space, defined by the mass of ALPs and their coupling to photons [2, 7, 8].
One of the predicted signatures of ALPs in the γ-ray emission is an imprint on the γ-ray spectra of AGN, in the form of "wiggles" in the spectrum. AGNs (see Sec. 3.2) are among the most promising targets for the study of particle acceleration in the Universe due to their high brightness and cosmological distances. Instruments covering the entire electromagnetic spectrum can ob-

[1] https://home.cern/science/experiments/cast

serve the same AGN, and the multi-wavelength data obtained can be used to model the broadband spectral energy distribution (SED) and shed light on the mechanism of the emission. In this work of thesis, VHE γ rays (photons) are used to search for signatures of ALPs in their spectra.
VHE γ rays emitted by AGNs or other astrophysical sources can be observed by the so-called IACTs (Imaging Atmospheric Cherenkov Telescopes) [9]. When γ rays enter the Earth's atmosphere, they interact with the present nuclei, generating a shower of particles which, because of their relativistic speed, emit a typical light flash called Cherenkov light. In a nutshell, the working principle of these telescopes is recording the Cherenkov light flashes and reconstructing the particle shower. IACTs are described in more detail in Sec. 3.1. Using the reconstruction software, energy, direction and various properties of γ ray can be obtained. In this thesis VHE γ-ray data from MAGIC telescopes are analysed. MAGIC telescopes is an array of two IACTs located on La Palma island the Canary Islands. For this study, one particular source has been considered, namely NGC 1275. NGC 1275 is an AGN located in the Perseus galaxy cluster. This choice was done based on the requirements of the ALPs study, which include strong magnetic field over great distances, high statistics and others that will be mentioned later in Sec. 3.2.1. Photon-ALP conversion will be predicted using the GammaALPs code developed by Manuel Meyer[2]. GammaALPs code is a Phyton code that uses the transfer matrix method for solving the equations of the photon-ALP system. Program and its principles are explained in Sec.4.3.1. Using different sets of parameters, mass of ALPs and their coupling to photons, the photon survival probability $P_{\gamma\gamma}$ is obtained from GammaALPs; then a convolution between $P_{\gamma\gamma}$ and a simple fit to the intrinsic spectrum of NGC 1275 is performed, in order to provide a description of the spectrum including ALPs predictions; and finally, a comparison between the convolution and the intrinsic spectrum is done. The intrinsic spectrum of the source is obtained using the standard MAGIC analysis chain with the suite `MARS` (MAGIC analysis and reconstruction software). Comparison between the intrinsic SED and ALPs prediction has been done. in order to measure the similarity between the intrinsic spectrum with and without ALPs predictions, squared residuals were calculated, although more precise quantification can be obtained using the likelihood which is planned to be calculated in the future.

In Sec. 2.1, the theory of axions and ALPs will be introduced. Sec. 3 is devoted to the role of axions and ALPS in astrophysics, including the experimental setup and general properties of the IACT telescopes used for

[2]https://github.com/me-manu/gammaALPs

obtaining VHE γ-ray data. Analysis of the data using the `MARS` software is described in Sec. 4, while in Sec. 5 the results of this study are presented and discussed. Conclusions are drawn in Sec. 6.

2 Axions and axion-like particles

2.1 Theory

2.1.1 $U(1)_A$ problem

Symmetries play a central role in physics. Among continuous and discrete ones, there are three prominent discrete symmetries in particle physics: parity (P-symmetry, P), charge conjugation (C-symmetry, C), and time (T-symmetry, T). For different processes there are many studies performed which include testing invariance on each of the symmetries mentioned. Two main conclusions are: first, that the time reversal is violated, and that the CPT theorem, which is the combination of charge conjugation, parity and time reversal symmetries, must hold. Of particular interest here is the combination of parity and charge conjugation, called CP symmetry. From the experimental evidence, it can be seen that the weak interactions violate this symmetry, but strong interactions don't, although there is nothing in the theory that forbids this. Moreover, in the quantum chromodynamics (QCD) theory which describes strong interactions between particles, there is a particular term in the Lagrangian that shows the presence of CP violation, which, at least so far, is not observed experimentally in processes with strong interaction. Lagrangian for QCD is:

$$\mathcal{L}_{\mathcal{QDC}} = -\overline{\psi}_i(i(\gamma^\mu \mathcal{D}_\mu)_{ij} - m\delta_{ij})\psi_j - \frac{1}{4}G^a_{\mu\nu}G^{\mu\nu}_a, \tag{1}$$

where ψ_i is the quark field, γ^μ are Dirac matrices, $\mathcal{D}_\mu$ is gauge covariant derivative, and $G^{\mu\nu}_a$ is the gluon field strength tensor. For N different flavors, in limit of $m \to 0$, Eq. 1 possesses the global symmetry $U(N)_V \times U(N)_A$. Considering that the masses of u and d quarks are much smaller than the dynamical scale of QCD theory, it is expected that the strong interactions will be approximately invariant on $U(2)_V \times U(2)_A$. What is known is that the vectoral subgroup of $U(1)_V$ symmetry is the real symmetry of QCD. Nonetheless, this is not the case with the axial component. What occurs is the production of quark $\langle \bar{u}u \rangle = \langle \bar{d}d \rangle \neq 0$ form, and axial symmetry is spontaneously broken [10]. As a consequence, the existence of Nambu-Goldstone bosons that are still not observed is expected. Weinberg called this the $U(1)_V$ problem [11]. This problem was solved by t'Hooft who used the QCD theory, namely by investigating its vacuum state [12, 13]. Considering vacuum's complex structure, QCD is not $U(1)_A$ invariant, although it seems like it is in limit of vanishing masses of quarks [10]. Solution of the $U(1)$ problem is proposed by using chiral anomalies of axial currents $J^5_{\mu\nu}$ [14]. Appliance of these anomalies on QCD vacuum causes occurrence of new term in $\mathcal{L}_{QDC}$:

$$\mathcal{L}_\theta = \theta \frac{g^2}{32\pi^2} G_a^{\mu\nu} \tilde{G}^a_{\mu\nu}. \tag{2}$$

This term violates two out of three discrete symmetries, parity P and time reversal T, but preserves charge conjugation C. That means that it violates CP symmetry. Eq. 2 depends on the angle θ. From experimental tests, done on the decay of a neutron, which as baryon should show possible existence of CP violation, one gets counter-intuitive results. Electrical dipole moment of the neutron,

$$d_n \approx e\theta(\frac{m_q}{M_N^2}), \tag{3}$$

shows the dependence on this same θ angle, and supposing the CP violation in the QCD one can expect that the value of d_n will be big. Experimental results [15] give its value,

$$|d_n| \approx 1 \times 10^{-26} \,\text{ecm}, \tag{4}$$

which demands for θ to be $< 10^{-9}$. Reason for such small value is not understood, although theory has the matching term, violation of CP in strong sector is still not observed. This is called the strong CP problem.
If one takes the electroweak sector into account, problem gets even worse. Applying the chiral transformation

$$q \to exp\,(i\beta\gamma_5)\,q \tag{5}$$

to quark flavors results with a new term in Lagrangian, similar to the one from QCD Lagrangian:

$$\frac{g^2\beta}{16\pi^2} G_a^{\mu\nu} \tilde{G}^a_{\mu\nu}. \tag{6}$$

This term is produced as a consequence of quantum loop corrections. Furthermore, when one calculates Noether's current for transformation in Eq. 5, new terms that vanish in case of massless quarks occur. That means that the QCD in it's classical form, is invariant to this transformation. What causes complications is that when quantum loop corrections are included, spontaneous symmetry breaking occurs, and term in Eq. 6 is produced. It can be shown that such transformations (Eq. 5) are needed in electroweak sector in calculating the masses of quarks:

$$\mathcal{L}_{mass} = \bar{q}_{iR} M_{ij} q_{jL} + \bar{q}_{iL} M^\dagger_{ij} q_{jR}, \tag{7}$$

were M is the quark mass matrix. To get the physical processes, one needs to diagonalize the matrix by using chiral transformation which causes the change of vacuum angle θ:

$$\theta_{eff} \to \theta + Arg\ \det M. \tag{8}$$

The solution of the strong CP problem is still a burning question of particle physics and the Standard Model of elementary particles. There are few proposals and suggested solutions which are explaining the absence of CP violation in the strong sector. First proposal is that there is a new, unconventional and unknown physics involved, still waiting to be explored. According to [10], this possibility is not favoured because of the lack of motivation for methods applied in articles using this approach but also new problems that arise while solving CP problem. Another solution is based on spontaneous breaking of CP symmetry. The reason why this solution is not widely accepted is the complex structure of models describing this small value of θ, ($\theta < 10^{-9}$), but also because the experiments mostly agree with the CKM matrix, which involves the mixing between quarks, and where CP symmetry is not spontaneously, but explicitly broken [10]. The third variant of the solution and probably the most known is the Peccei-Quinn theory, which will be briefly explained in the next section.

2.1.2 Strong CP problem - Peccei-Quinn mechanism and axions

In the QCD context it is believed that the strong interactions are the consequence of non-Abelian vector gluons coupled to massive quarks. In such theories CP invariances require special choice of parameters [1, 16]. In an article from 1977 [1], R. D. Peccei and H. R. Quinn proposed a dynamical solution of strong CP problem and showed that the CP invariance of the strong interactions is actually "natural". "Natural" means satisfying the condition that at least one flavor of quarks acquires its mass from Yukawa coupling to a scalar field. One of the properties of that scalar field is that it has a nonzero vacuum expectation value, and its Lagrangian has the $U(1)$ invariance which involves all Yukawa couplings. According to t'Hooft, gauge configurations with non-trivial topologies possess a parameter θ which is not occurring in original Lagrangian. θ affects the choice of vacuum and for every different choice of θ one can get different theory from any given Lagrangian [1, 16]. R.D.Peccei and H.R.Quinn investigated such theories, using that at least one of fermion flavor acquires mass by Yukawa coupling and color-singlet scalar field with vacuum expectation value different from zero [1, 16]. Important is that the Lagrangian and the effective potential of the scalar

field chosen do not have the same symmetries. That means that for various values of scalar expectation value, one has a phase which corresponds to the minimum of the potential. This phases are present in fermion mass terms and by using chiral transformations they can be driven to zero.
In year 1977. R.D.Peccei and H.R.Quinn, showed in [1] that one of the potential solutions to the strong CP problem lays in existence of chiral $U(1)$, today known as $U(1)_{PQ}$ symmetry. In case that this symmetry exists and if the Lagrangian of the Standard Model is invariant under it, value of the θ_{eff} can be driven to zero using the chiral transformations mentioned before (see Eq. 5)[1, 16]. Although this symmetry is not exact, Peccei and Quinn showed that when symmetry is spontaneously broken, θ_{eff} can be driven to zero and in that case the existence of Nambu-Goldstone boson, axion, is expected, as suggested by S.Weinberg and F. Wilczek in 1978 [17, 18]. In order to go deeper into this problem and explain why this solution to the strong CP problem is rather accepted, a brief derivation of this model will be provided, following the instructions from original paper by Peccei and Quinn. In it, existence of only one fermion flavor and complex scalar field with one color-singlet is assumed. Lagrangian for this theory is:

$$\begin{aligned}\mathcal{L} = &-\frac{1}{2}F_{\mu\nu}^{\ a}F^{\mu\nu}_{\ a} + i\bar{\psi}D_\mu\gamma^\mu\psi + \bar{\psi}[G\varphi\frac{1}{2}(1+\gamma_5) + G^*\varphi^*\frac{1}{2}(1-\gamma_5)]\varphi \\ &- |\partial_\mu\varphi|^2 - \mu^2|\varphi|^2 - h|\varphi|^4; \mu^2 < 0,\end{aligned} \tag{9}$$

and it is invariant under chiral rotations:

$$\psi \to exp(i\sigma\gamma_5)\psi, \quad \varphi \to \exp(-2i\sigma)\varphi. \tag{10}$$

Chiral rotation here changes the parameter θ:

$$\theta \to \theta - 2\sigma. \tag{11}$$

It can be shown that for any value of θ one gets equivalent theory.
Derivation of CP conservation in this theory begins with functional for Green's function in θ vacuum [1, 16]:

$$\begin{aligned}Z_\theta(\theta,\theta^*) &= e^{iW(s)} \\ &= \sum_q e^{i\theta q}\int (dA_\mu)_q \int d\psi \int d\bar{\psi}\int d\varphi \int d\varphi^* \\ &\times exp\Big[\int d^4(\mathcal{L} + \mathcal{J}\varphi + \mathcal{J}^*\varphi^*)\Big].\end{aligned} \tag{12}$$

Then one defines the scalar vacuum expectation value as:

$$\frac{1}{Z_\theta}\frac{\delta Z_\theta}{\delta\mathcal{J}}\bigg|_{\mathcal{J}=\mathcal{J}^*=0} = \langle\varphi\rangle = \lambda e^{i\beta}, \tag{13}$$

where constants λ and β are real. Furthermore, new variables are introduced:

$$\varphi = e^{i\beta}(\lambda + \rho + i\sigma). \tag{14}$$

Now one can write generating functional as:

$$Z_\theta(\mathcal{J}, \mathcal{J}^*) = \sum_{q=-\infty}^{\infty} \left(\int dA_\mu \right)_q e^{iq\theta} \int d\psi \int d\bar{\psi} \int d\varphi \int d\varphi^* exp[\mathcal{L}(\varphi\varphi^*)]$$
$$exp\left[+ \int d^4x (-\frac{1}{4}FF + i\bar{\psi}\not{D}\psi) \right] \times \sum_{n,m} \frac{1}{n!m!} \left[\int d^4x \, \bar{\psi} \, G \, \varphi \left(\frac{1+\gamma_5}{2} \right) \psi \right]^n$$
$$\int d^4x' \left[\bar{\psi} \, G^* \varphi^* \left(\frac{1-\gamma_5}{2} \right) \psi \right]^m exp(\mathcal{J}\varphi + \mathcal{J}^*\varphi^*). \tag{15}$$

This is based on knowing that the contributing terms over each sector are the ones with $n - m = q$, as a consequence of changes in chirality introduced by presence of pseudoparticles. After integration of vector and fermion fields:

$$Z(\mathcal{J}, \mathcal{J}^*) =$$
$$\int d\rho \int d\sigma \{ A_0(\rho, \sigma^2) + \sum_n A_n(\varphi\varphi^*)[G \, e^{i\theta}\varphi]^n + A_n^*(\varphi\varphi^*)[G^* e^{-i\theta}\varphi^*]^n \}$$
$$\times \, exp[\mathcal{J}e^{i\beta}(\lambda + \rho + i\sigma) + \mathcal{J}^* e^{-i\beta}(\lambda + \rho - i\sigma)], \tag{16}$$

where A_n are polynomials of the form:

$$A_n(\varphi\varphi^*) = \sum_m \prod_{i=1}^{m} \left[\int dx_i \int dy_i \varphi(x_i)\varphi^*(y_i) \right] c_m^n(x_i, y_i). \tag{17}$$

c_m^n are real functions depending on $|G|^2$, μ, h, but not on β and λ. The terms proportional to G^n are coming from fermion zero eigenmodes in the $q = n$ sector, while the ones proportional to $(G^*)^n$ are from $q = -n$ sector [1, 16]. Using the new variable:

$$\alpha = arg[Ge^{i(\theta+\beta)}], \tag{18}$$

Eq. 16 can be rewritten:

$$Z(\mathcal{J}, \mathcal{J}^*) = \int d\rho \int d\sigma \{ A_0(\rho, \sigma^2) + \sum_n [F_n \, (\rho, \sigma^2) \cos n\alpha - \sigma G_n \, (\rho, \sigma^2) \sin n\alpha] \}$$
$$\times \, exp[\mathcal{J}e^{i\beta}(\lambda + \rho + i\sigma) + \mathcal{J}^* e^{-i\beta}(\lambda + \rho - i\sigma)], \tag{19}$$

where F_n is real, and σG_n real is imaginary part of $A_n|G|^n(\lambda+\rho+i\sigma)^n$. Furthermore, for λ and ρ conditions are:

$$\langle\rho\rangle = \int d\rho \int d\sigma\rho(A_0 + \sum_n F_n \cos n\alpha) = 0 \tag{20}$$

$$\langle\sigma\rangle = \int d\rho \int d\sigma\sigma^2 \sum_n G_n \sin n\alpha = 0, \tag{21}$$

since they have zero expectation values of vacuum. First equation can be satisfied for any α while second requires α to be $\alpha = 0, \pi$. In order to find a CP invariant theory, one needs to deduce the nature of these two points. One of them is minimum and for α to be zero, certain range of parameters G, h and λ is needed. They can be found by examining the scalar potential. For this purpose, this can be done only in leading approximation for small G i h [1, 16]. Using the approximation for G i h scalar potential becomes:

$$V_\theta = U(\varphi) - K|G\varphi|\cos\alpha, \tag{22}$$

where U is:

$$U(\varphi) = \mu^2\varphi^*\varphi + h(\varphi^*\varphi)^2, \tag{23}$$

and K is a real, positive constant. It is seen that Eq. 22 does not posses the same $U(1)$ symmetry as required in the original Lagrangian. This explains the absence of the Goldstone boson expected [1, 16]. What happens is that the fermions acquire the mass as visible in the mass terms:

$$\lambda\bar{\psi}[Ge^{i\beta}\frac{1}{2}(1+\gamma_5) + G^*e^{-i\beta}\frac{1}{2}(1-\gamma_5)]\psi. \tag{24}$$

As explained, using the chiral rotation ($exp[i\gamma_5\frac{\theta}{2}]$) of fermion fields this mass becomes real, and change in θ angle is produced: $\theta \to \theta' = \theta - \theta = 0$.
Generalization of this derivation to more flavors of fermions is similar. In summary, it is possible to find the needed range of parameters in order to obtain the minimum of the scalar potential which gives CP conservation. New condition, that corresponds to $\alpha = 0$ is:

$$arg\left\{\prod_{i=1}^{m}(G_i\, exp[i\beta_{ji}])exp[i\theta]\right\} = 0, \tag{25}$$

where G_i are Yukawa couplings of i-th fermion flavor for j-th neutral scalar. In the end, rotating fermion fields using the chiral rotation, it generalizes to $\sum_i \eta_i = \frac{\theta}{2}$ and makes the masses real. In conclusion, one gets a CP invariant

theory with $\theta_{eff} = 0$.
Few months after this discovery, spontaneous breaking of $U(1)_{PQ}$ symmetry was proposed [17, 18] and as its consequence, the existence of the Nambu-Goldstone boson, the axion, was postulated.

2.2 Axions and ALPs

The new chiral $U(1)_{PQ}$ symmetry introduced, brought changes into new Lagrangian. What is found, is that this new symmetry has to be spontaneously broken, which means one should expect the existence of Goldstone boson and some new contribution in the Lagrangian. This new boson is called axion and the new term mentioned is CP-conserving axion field. Due to chiral $U(1)_{PQ}$ transformation, axion field is transformed:

$$a(x) \to a(x) + \alpha f_a, \tag{26}$$

where f_a is the scale of $U(1)_{PQ}$ spontaneous symmetry breaking [17]. From the new Lagrangian, $U(1)_{PQ}$ invariant,

$$\mathcal{L}_{eff} = \mathcal{L}_{SM} + \theta_{eff}\frac{g^2}{32\pi^2}G_a^{\mu\nu}\tilde{G}^a_{\mu\nu} - \frac{1}{2}\partial_\mu a \partial^\mu a + \mathcal{L}_{int}\left[\frac{\partial^\mu a}{f_a};\Psi\right] + \xi\frac{a}{f_a}\frac{g^2}{32\pi^2}G_a^{\mu\nu}\tilde{G}^a_{\mu\nu}, \tag{27}$$

in combination with Eq. 2, one can write the effective potential of axion:

$$V_{eff} = (\theta_{eff} + \xi\frac{a}{f_a})\frac{g^2}{32\pi^2}G_a^{\mu\nu}\tilde{G}^a_{\mu\nu}. \tag{28}$$

If one finds it's minimum and expands the potential around it:

$$m_a^2 = \left\langle \frac{\partial V_{eff}^2}{\partial a^2} \right\rangle = -\frac{g^2\xi}{f_a 32\pi^2}\frac{\partial}{\partial a}\langle G_a^{\mu\nu}\tilde{G}^a_{\mu\nu}\rangle\Big|_{\langle a\rangle = -\frac{f_a}{\xi}\theta_{eff}}, \tag{29}$$

where m_a is the mass of the axion [10]. As noted, axions arise as a consequence of spontaneous breaking of additional global symmetries added to the Standard Model. In general case, these pseudo-Nambu-Goldstone bosons created are called ALPs. In addition, they are connected to axions, who are solving the strong CP problem, as explained before. Difference between them, or as one may say, "advantage" of ALPs is that their mass m_a and coupling to photons $g_{a\gamma\gamma}$ are not dependent, which makes the experimental search for them more appealing.

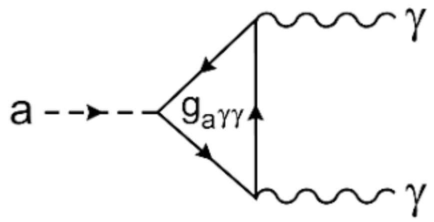

Figure 1: Feynman diagram of photon-ALP coupling.

2.3 Axion and ALPs searches

In this section interaction of ALPs with photons will be briefly explained. This interaction is the main tool of researches in the hunt for ALPs.:

$$\mathcal{L}_{a\gamma\gamma} = -\frac{g_{a\gamma\gamma}}{4} F_{\mu\nu}\tilde{F}_{\mu\nu} a = g_{a\gamma\gamma} \vec{E} \cdot \vec{B} a, \tag{30}$$

where $g_{a\gamma\gamma}$ is the ALP-photon coupling, $F_{\mu\nu}$ the strength tensor of electromagnetic field, $\tilde{F}_{\mu\nu}$ its dual, and a is the axion field with mass m_a. The Feynman diagram for this interaction is shown in Fig. 1. This effect, explained as axion-photon conversion, occurs in strong magnetic fields and it is the basis of many experiments in search for ALPs. Several experiments are performed exploiting this effect. Some of them are conducted in laboratories as light-shining-through-the-wall experiments, laser beam regeneration experiments and some other in which the problem of axion-induced birefringence of the vacuum is addressed, such as ALPS I [19] and OSQAR [20] at CERN. There are also experiments that are using helioscopes in the search for solar axions and among them, the most known is probably the experiment CAST [4]. As proposed by [21], another observable phenomenon could be also the conversion of axions into electromagnetic power in a resonant cavity. This study laid theoretical ground for modern experiments such as ADMX (Axion Dark Matter eXperiment) [3]. Since ALPs are connected with the spontaneous symmetry breaking, they could have been produced in the early Universe via ”misalignment” mechanism. As such they could represent a substantial fraction of Dark Matter. Moreover it is found [22] that in order to explain current amount of the Dark Matter with ALPs, axion coupling, dependent on mass of axions has to be

$$g_{a\gamma\gamma} < 10^{-12} \left[\frac{m_a}{1 \text{ neV}}\right]^{1/2} \text{GeV}^{-1}. \tag{31}$$

In this work the results of the above mentioned experiments will not be investigated in detail, since focus will be on the astrophysical aspect of this

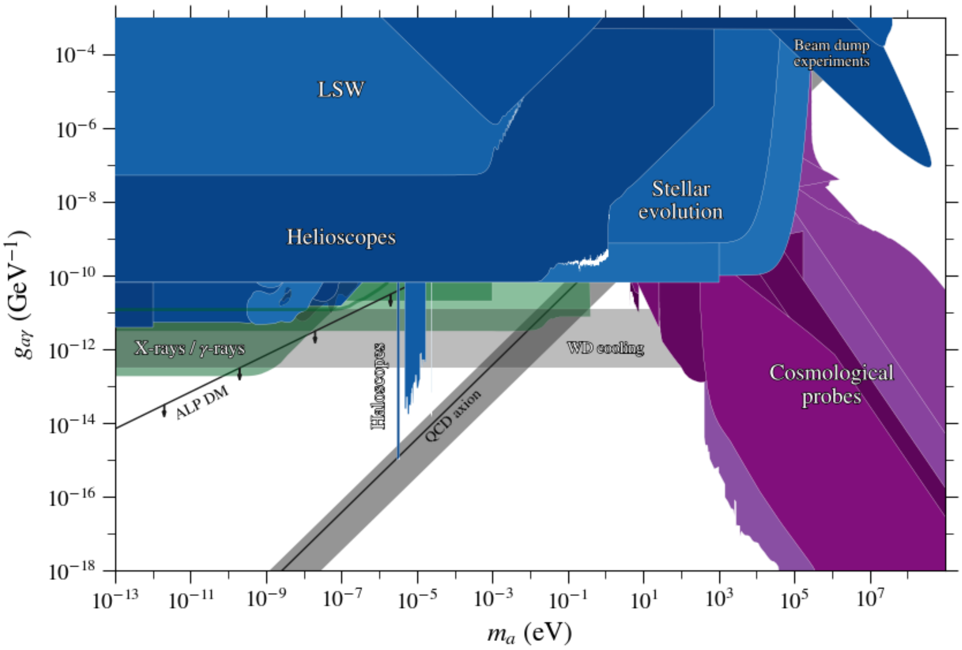

Figure 2: ALPs parameter space[3].

search. ALPs parameter space for the mentioned experiments with current constraints is shown in Fig **??**.

Part of ALPs parameter space considered here and available for probing with γ-ray experiments can be seen in Fig. 15. Of course, this part of ALPs parameter space currently available is expected to be broadened with new upcoming generation of γ-ray telescopes such as CTA (Cherenkov Telescope Array) [23].

[3] `https://github.com/me-manu/gammaALPsPlot`

3 Axions in astrophysics

A very interesting aspect of the study of axions in astrophysics is their conversion to photons in strong magnetic fields. In that way they can affect the spectra of astrophysical objects, as the one which will be investigated in this work. There is another well-known effect which influence the spectra of AGNs in the γ-ray range, and that can be significant in the VHE γ-ray range: the absorption of γ rays by the photons of the extragalactic background light (EBL). Many models [24, 25, 26, 27] have been developed to describe this effect and to apply a correction on the VHE γ-ray spectra from AGNs. After the deabsorption performed by those models, the spectrum in the VHE γ-ray range is called "intrinsic" because it represents the spectrum "at the origin" before the EBL interaction. Among the different models, for this study [27] is used. When converted to ALPs, photons can elude the EBL absorption and be converted back into photons. In this way, an higher (with respect to the intrinsic spectrum corrected for EBL) flux of VHE photons than expected can be observed. Another aspect of photon-ALP mixing are the imprints that they could leave on γ-ray spectra of astrophysical objects under the form of oscillations or "wiggles". Such effect would impose irregularities in the spectrum around a critical energy E_{crit}, above which photon-ALP mixing becomes maximal, if mass of ALPs is sufficiently small $m_a \lesssim 1\ \mu eV$.

$$E_{crit} \sim 2.5 \text{ GeV} \, \frac{|m_{a,neV}^2 - \omega_{pl,neV}^2|}{g_{11} B_{\mu G}}, \tag{32}$$

where $\omega_{pl,neV}$ is the plasma frequency in units of neV, $B_{\mu \mathrm{G}}$ is magnetic field in microgauss and $g_{11} = g_{a\gamma\gamma}/10^{-11}$ GeV^{-1}. When investigating axions and ALPs, great care has to be taken considering how to represent the magnetic fields. As reported by P. Sikivie in [21], there are several ways this problem can be and was approached before. First is that the photon-ALP conversion was assumed only in environments around γ-ray source, meaning in its magnetic field and in the magnetic field of Milky Way [28, 29, 30]. This particular point can get rather complicated, since information about the magnetic fields surrounding astrophysical objects such as AGNs are not often very detailed. Second approach is consisted in including photon-ALP conversion in random extragalactic magnetic fields [31, 24]. In the latter case, the challenge is represented by the magnetic field strength, since by this kind of assumptions intergalactic magnetic field strength is restricted to B $\sim (0.1 - 1)$ neV, which is still not experimentally confirmed. Other methods are including combinations of two previously mentioned mechanisms [5]. For the present work, approach of [32] is used, in which conversion of photons to ALPs is studied in galaxy clusters, and combined with the back-conversion from ALPs to photons in the magnetic field of Milky Way. The advantages of this approach are that magnetic fields in clusters of galaxies and in the Milky Way are rather known and EBL absorption is strongly reduced when dealing with very close clusters as Perseus (in general the EBL absorption in VHE γ rays is negligible for redshifts <0.3). In Sec. 3.1 the experimental setup used for this work will be explained, including the working principle of MAGIC telescopes, and the data analysis chain will be described in Sec. 4. The modelling of photons-ALPs oscillation applied in this study will be described in details in Sec 4.3.

3.1 IACT telescopes - MAGIC

IACTs (Imaging atmospheric Cherenkov telescopes) are instruments suitable for the detection of VHE γ rays, highly energetic photons which can be produced in the environment of astrophysical objects such as AGNs, supernovae, binary stars, pulsars... Their energy is in the range $\sim$ 50 GeV - 50 TeV. The three major arrays of IACTs are the High Energy Stereoscopic System (H.E.S.S.) [33], the Very Energetic Radiation Imaging Telescope Array System (VERITAS) [34], and last but not least, MAGIC. The next generation of IACTs is the (CTA) [23]. CTA currently has one prototype of Large Scale Telescope (LST) (out of three types of telescopes that will be build), located near MAGIC telescopes on the Canary island of La Palma. The detection of VHE γ rays from astrophysical sources can be complicated since their flux is rapidly falling with the increase of the energy. Due to high energies, these particle showers, show big energy dispersion. For that reason, relatively big detection areas are needed, so space telescopes with relatively small collection areas (~ 1 m^2) are ineffective in this energy range. In order to detect particles of such high energies, IACTs are needed. IACTs have diameter of ~ 10 m and they use Earth's atmosphere as a detection medium. Exploiting stereoscopic approach and great angular resolution (better than $0.1°$) IACTs have, one can distinguish between γ-ray and hadronic showers very accurately, significantly reducing the background [9]. The pioneer of VHE γ-ray observation was Whipple imaging atmospheric telescope with 10 m radius, predecessor of today's VERITAS. In 1989, Whipple detected the first TeV γ-ray source [35]. This source is Crab Nebula, a supernova remnant with a pulsar in its center. Crab Nebula is a standard candle in MAGIC analysis, due to its brightness and vicinity. In this thesis, data collected by MAGIC telescopes will be analyzed. MAGIC collaboration includes scientists from 17 research institutes from 9 different countries. With energy range $\sim$ 25 GeV - 30 TeV, MAGIC is collecting data from supernova remnants, AGNs, γ-ray bursts and looking for answers to most prominent questions in astroparticle physics.

3.1.1 Cherenkov light

The most usual comparison used in describing Cherenkov radiation is the one with the sonic boom that occurs when airplane travels faster than sound in air and as a result, a Mach cone is produced.
When particles are travelling in a medium with a speed higher than speed of light in that medium, Cherenkov radiation is emitted. This is what precisely happens when VHE photons enter the Earth's atmosphere. The photons interact with the molecules of the upper Earth's atmosphere producing cascades of secondary particles which constitute an electromagnetic shower. The Cherenkov radiation is observed as a faint blue flash, lasting around billionths of a second [36], too fast to be captured by human eye. The Cherenkov radiation was named after Pavel Alekseyevich Cherenkov, first scientist who studied this effect experimentally [37, 38]. Before him, this effect was also noticed by Marie and Pierre Curie, who observed blue light coming from transparent materials containing uranium salts. After P. A. Cherenkov, in 1937, I. M. Frank and I. E. Tamm explained this effect based on the Maxwell's equations [39], while the first to explain Cherenkov radiation in air was P. M. S. Blackett in 1948 [40]. A charged particle moving in dielectric medium interacts with other particles present in it. These particles are excited in higher states, so when returning to ground state, they are emitting photons. In case the speed of particle is higher than the speed of light in that medium, $v > c$, emitted photons are adding up and creating coherent radiation. This radiation is emitted at angle θ in respect to direction of the particle, ultimately giving the Cherenkov radiation shape of a cone, as seen in Fig 3. θ_c angle is function of air density and height of the emission, so it increases with decrease of the height. It is given by:

$$\theta_c = \frac{1}{\beta n}, \tag{33}$$

where $\beta = \frac{v}{c}$, v is the speed of particle, and n is refractive index of the medium, in this case, air. The emitted Cherenkov radiation is additionally affected by Coulomb scattering of the produced charged particles in a way that it changes the angle of the shower. So in order to find the distribution of secondary particles produced in the shower, one has to take it into account. Moreover, Cherenkov light spectrum has a peak at short wavelengths [9]. From the source spectrum given by Frank-Tamm equation [39]:

$$\frac{d^2 N_{\mathrm{ph}}}{dx\, d\lambda} = \frac{2\pi\alpha}{\lambda^2} \sin^2\left(\theta_{\mathrm{c}}\right) \tag{34}$$

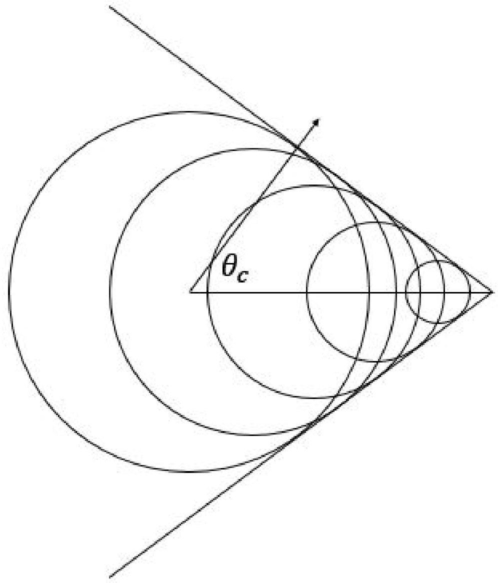

Figure 3: Cherenkov radiation cone.

one can obtain number of photons produced N_{ph} in wavelength λ interval on a path of length dx and Cherenkov angle θ_c. Other than mentioned, atmosphere also modifies the spectrum and causes dependence on positioning of the telescope, mainly height on which observations are performed, zenith angle and height of shower maximum. When dealing with not optimal weather conditions, especially for the presence of thick clouds, LIDAR (light detection and ranging) is used to measure the transmission across the atmosphere and then in a later step corrects the energy reconstruction of the showers at a software level.
Cherenkov detectors are divided in two main groups, sampling and imaging counters, and as already introduced, MAGIC belongs to the latter one.

3.1.2 Working principle of MAGIC

MAGIC site is located on La Palma island on Canarian islands on altitude of 2200 m. As mentioned, it is consisted of two 17 m IACTs operating from 2004 (the second telescope was built in 2009). MAGIC telescopes are shown in Fig. 4. Telescopes can operate separately or in stereoscopic (stereo from now on) mode, observing the same source simultaneously. The telescopes are altitude-azimuthal, which makes tracking during long exposures

[4]credit: Giovanni Ceribella

Figure 4: MAGIC telescopes[4].

more feasible [9]. Stereo mode is great advantage of IACT arrays because it increases flux sensitivity, reduces energy threshold and improves angular resolution by reduction of the background [9]. Each MAGIC telescope is composed by two main parts, a large reflector and a fast photo-multiplier camera in the focal plane of the reflector. MAGIC reflectors are mirror dishes with a size of 236 m^2 assembled by almost 1000 hexagonal aluminum and glass mirrors. Both cameras have a high resolution of $3,5°$ and contain 1039 photo-multiplier tubes. Photography of MAGIC camera is shown in Fig. 5. When a γ ray enters the Earth's atmosphere, it interacts with the molecules present in the atmosphere and decays into an e^-e^+ pair. Furthermore, since these particles have charge, they are deflected by another charge and consequently they lose energy, producing bremsstrahlung radiation and new γ rays. This process continues until the energy of the produced particles is not big enough to provide production of new particles. Showers can be initiated by different kind of particles as well. When cosmic-rays, meaning charged particles, enter the Earth's atmosphere, they interact with particles in the atmosphere and decay, mostly into pions (π^0, π^+, π^-). Subsequently pions, depending on their charge, decay into differently charged muons (μ^-, μ^+), which, if energetic enough, can reach the Earth's surface. This process causes the biggest part of background in γ-ray astronomy. Difference in the develop-

Figure 5: The camera of MAGIC-II (credit: the MAGIC collaboration).

ment of γ-ray and hadronic shower can be appreciated in Fig. 6. MAGIC and other IACTs use Monte Carlo simulations to differentiate γ-ray showers from cosmic-ray (usually called hadronic) showers. In 1963, J.V. Jelley and N.A. Porter proposed that the nature of shower can be distinguished by the shape of the Cherenkov image obtained in the camera [41]. They conclude that the cosmic ray image has rather complicated shape, while the image produced by a muon has a circular shape. On the other hand images produced by γ ray induced showers will have rather elliptical-like shape. Such a difference can be seen in Fig. 7. Also, based on the orientation of the image, it is possible to reconstruct the direction of the incoming particle, and to reconstruct its energy from the intensity. In order to separate and characterise γ-ray images in contrast to hadronic ones, one chooses set of quantities called Hillas parameters [42]. Some of the most important parameters are width, length and size of the image. Putting constraints on them, good separation between γ and hadronic events is achieved. This procedure has few different steps, first, while recording, even at the trigger level, when threshold is exceeded in few pixels in the camera, based on the conditions, difference is determined. Considering MAGIC, there are different types of triggers, including triggering only one of the telescopes, or simultaneously triggering both, and depending on how much neighbouring pixels are triggered. Next step includes selecting data by determining Hillas parameters. Here again, as already said, stereo observation mode provides more detailed reconstruction of the shower, morphology of the source and reduces background impact.
Further analysis is carried out by the analysis software, in MAGIC called `MARS`. `MARS` contains $\sim$ 36 executable programs and macros. With it, so called "raw" data can be analyzed to ultimately produce the light curve, spectrum and other high level analysis output. Depending on whether both

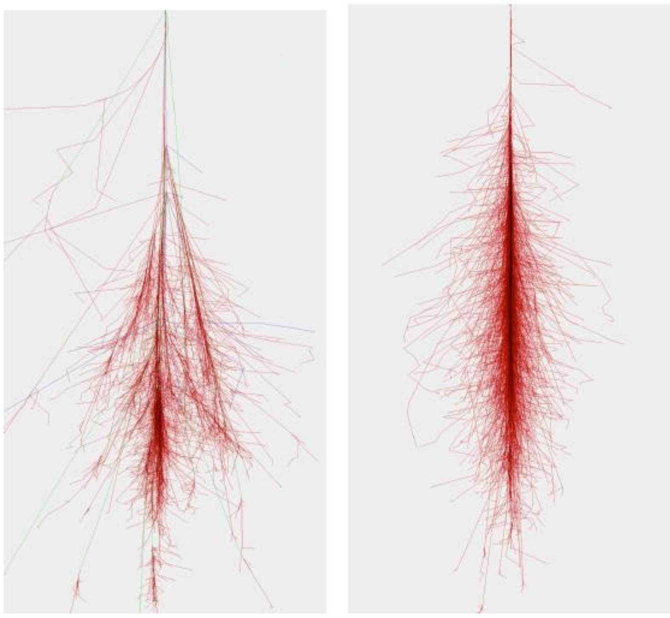

Figure 6: Hadronic (left) and γ-ray (right) shower development in the atmosphere (adopted from http://lapp.irb.hr/publications/DarioPhD.pdf).

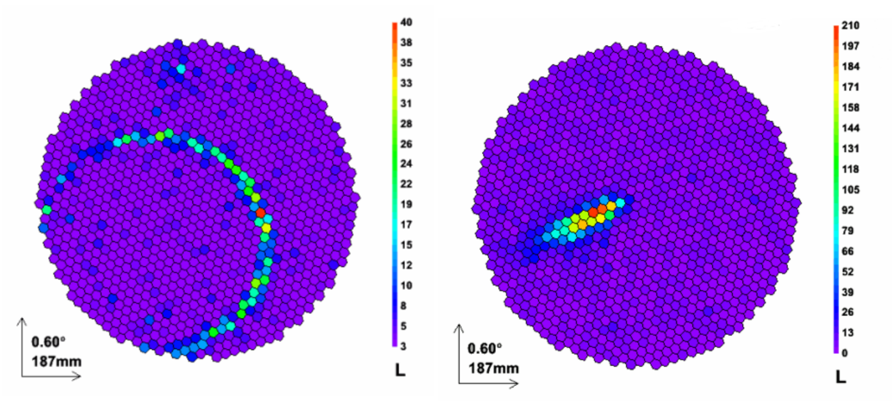

Figure 7: Hadronic (left) and γ-ray (right) event images in the camera (from the MAGIC collaboration).

or only one telescope is used for observation one can perform stereo or mono analysis, respectively. In both cases, analysis chain is defined and needed programs are provided. In this work of thesis, standard stereo analysis was used and its scheme and the procedure will be explained in greater detail in Sec.4.

3.2 Source - active galactic nuclei

Before starting with the data analysis, source has to be chosen. In this case, AGN is considered. AGN is a supermassive black hole in the center of a massive galaxy ($10^6 - 10^{10}\ M_\odot$). Recognized as very bright sources, their luminosity varies on a scale from hours to days and can outshine the whole galaxy (quasars). Although they are usually connected with presence of relativistic jet, only ~ 10 % of AGNs have it, while only ~ 1 % supermassive black holes even have an accretion disk, caused by a strong gravitational field attracting the surrounding material, magnetized and active. Among other characteristics important to acknowledge are broad-line and narrow-line regions, corresponding to emission from high and low velocity gas, respectively. Also, hiding the narrow line region there is torus of gas and dust, especially present in spectra of some type of AGNs in form of strong radio and X-ray radiation. There is no firmly established classification of AGNs and there is no good explanation for it. With that said, the liberty of using one particular classification will be taken here. Based on the direction from which it is observed, meaning based on it's orientation in respect to the field of view, one can distinguish different types of AGNs, as shown in Fig. 8. This model is usually called the "unified model" of AGN [43]. In this context, if the AGN possessing relativistic jet is pointing towards the observer, it is called blazar. Blazars are found to be very variable over almost whole electromagnetic spectrum [44]. They are subsequently divided in few types, in e.g. BL-Lacs (BL Lacertae) and FSRQ (Flat Spectrum Radio Quasar). BL-Lac is a highly active blazar, characterised by weak emission lines and rather "poor" spectral distribution, as no special features are observed over the entire electromagnetic spectrum. Also, they make the biggest fraction of so far observed AGN objects and they are present on the redshift z ~ 0.3. In contrast to them, FSRQs are recognizable by strong emission lines and spectrum dominated by the radiation of torus of gas and dust, usually present at bigger distances (z $\sim (0.6 - 1.5)$). Quasar part of the name is because of big luminosity that overcomes the luminosity of the whole galaxy in which AGN is situated in. On the other side, there are AGNs whose jets are not aligned with the line of sight (usually under angle of $15°$ - $45°$ in respect to line of sight [45]). One of them are called radio galaxies. They are characterised by

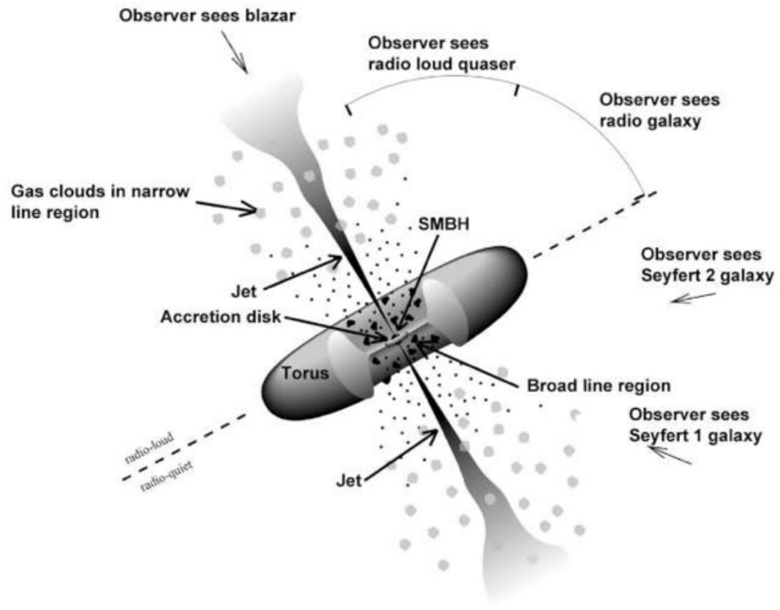

Figure 8: Unified model of AGNs (from https://fermi.gsfc.nasa.gov.).

strong radio emission due to synchrotron emission of charged particles and they do not show any broad emission lines in the spectrum. When considering spectra of AGNs there are few different models of describing the observed radiation. Most generally these are divided in two groups, hadronic and leptonic models, roughly differentiated by the amount of high energy protons ($E > 10^{19}$ eV) present. With their characteristics, AGNs are listed as one of the most violent sites in the Universe, and as such, are great candidates for acceleration of particles. Actually, these objects could explain the observation of the most energetic particles detected, with energies $> 10^{21}$ eV. SED of these objects has two "bumps", one on the lower, and one on the higher energies as in Fig. 9. Because of such features, distributed over the whole electromagnetic spectrum, AGNs are also great sources to apply the multi-wavelength astronomy. Based on the current models provided, first bump on lower energies is explained by synchrotron emission of high energy electrons, and second one on higher energies, by Compton emission, or sometimes combined with synchrotron emission (synchrotron-self Compton). SED of AGN can show certain irregularities and reduction of photon flux, which, as already mentioned cannot entirely be explained by effects such as EBL absorption. On the other side, pseudo-particles such as ALPs can suffer coupling to photons in strong magnetic or electric field. In that way they could be accounted for reduction of photon flux, consequently causing oscillations

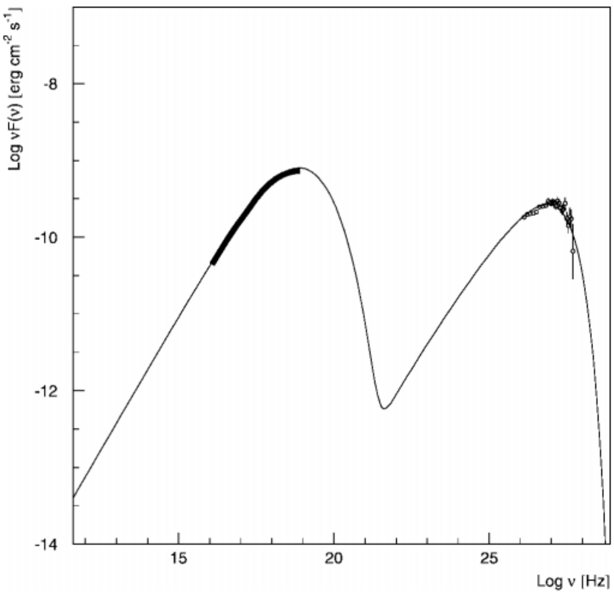

Figure 9: SED of Markarian 501 [46].

in the AGN spectra.

3.2.1 NGC 1275

NGC 1275 is an AGN classified as radio galaxy in the center of the Perseus cluster of galaxies. It possesses extended relativistic jet with morphology [47]. It is positioned on a redshift z $\sim$ 0.017559. First it was detected as high-energy source [48] with spectrum well fitted with the power-law. During the years it showed variability on scales of months to day and as such, power law fit of the spectrum was supplemented with an exponential cut-off, while also harder-when-brighter correlation was found [49]. As it's located in the cluster of galaxies, it is surrounded by strong magnetic field and in that way checks one of the conditions needed to conduct this study. NGC 1275 has a long tradition of observations using MAGIC telescopes and for that reason there is a lot of data available for analysis. Through the years it has been analyzed in dark matter studies (in e.g. [50]), galaxy clusters studies (in e.g. [51]) and etc. Due to its relative proximity ($\sim$ 75 Mpc), effects of the EBL are almost negligible so they do not significantly alter the spectrum.

[5] credit: NASA, ESA, NRAO and L. Frattare (STScI)

Figure 10: NGC 1275 multi-wavelength composite image[5].

4 Analysis

4.1 Data sample

MAGIC array started operating in 2003 with a single telescope (MAGIC-I) and in 2009 another identical telescope was added (MAGIC-II). Since then, the array can operate in stereo mode, although mono data from single telescopes can still be recorded and analyzed. MAGIC underwent a major hardware upgrade in 2011 and 2012, when camera and trigger system of MAGIC-I were upgraded, and both telescopes were provided with a new readout system. After the upgrade, a new study on the performance was conducted [52, 53]. MAGIC observations through the years are divided in several analysis periods and each of them have specified conditions that should be considered during the analysis. So far, there are 14 analysis periods. For this study, data from two analysis periods are analysed: 6^{th} and 7^{th} period, named ST_03_06 and ST_03_07, for an amount of 9.0 hours and 45.1 hours, respectively. The first period analysed did not show any particular high activity. The latter one instead, contained a very bright flare in date 31 Dec 2016 which is used for this study, because of the high significance of the signal. In this thesis only results from the latter period, ST_03_07, will be presented.

ST_03_07 includes data taken during the period from 29 Apr 2016 to 2 Feb 2017, and the results of data analysis of MAGIC data from NGC 1275 obtained during this observational period were already presented in an earlier work [54], which was focused on the fast variability of the source and on the different emission scenarios studied in a multi-wavelength context. In [54] it was concluded that the very bright γ-ray flare observed in date 31 Dec 2016 was challenging all of the already existing models for fast variability in the VHE γ-ray range. In this work, the same flare is studied but with a different focus: goal is to use the predictions of photon-ALP coupling to possibly explain the oscillations in the spectrum of NGC 1275 during the flaring state, or to add constraints on the ALPs parameter space, if the outcome is not in favour of photon-ALP conversion. Data of NGC 1275 from the ST_03_07 analysis period includes 27 days, with (45.1 hours) of observational time. Details on the weather conditions and on the data taking are stored in files known as runbooks and superplots for each night of observation. Studying those conditions, quality cuts on sample are applied, referring to atmospheric transmission limit that was set on 0.7 for 3 km, 6 km, 9 km and 12 km height, excluding 1.8 hours of data on the basis of bad weather or technical conditions that affected the observations and possibly the data, if recorded in such conditions. The data analysed, passed the quality cuts amounts to 43.3 hours.

4.2 MAGIC analysis chain

The official software for MAGIC analysis is named `MARS`. `MARS` includes over 36 programs and macros for data analysis, one could call it "the tool box of MAGIC". For this study, stereo data, stored in files called Superstar, is used. `MARS` analysis is based on C++ and the data analysis program `ROOT`, so all the files used for the analysis chain are `ROOT` files. The stereo analysis in MAGIC follows several steps. Superstar level is the starting point, as it is common for standard analysis of MAGIC data.

In Fig. 11, the stereo MAGIC analysis scheme is shown, where green color represents different type of data, blue marks are `MARS` programs and yellow ones are scientific results of high level analysis.

After the data selection, additional cuts on the data need to be performed. Cuts on the superstar data are made using the executable `Quate`. `Quate` calculates the average of some parameter, or more parameters sets, but also performs data quality selection. Depending on the needs and goals of the analysis, data cuts are performed. In this work, greater attention was brought to cut on the weather conditions excluding cloudy weather which could compromise the reconstruction of the energy spectrum. Information about the atmosphere condition are provided by the LIDAR, and they have to be checked during the data selection in order to get the best quality data. For

[6] MAGIC Data Analysis Manual

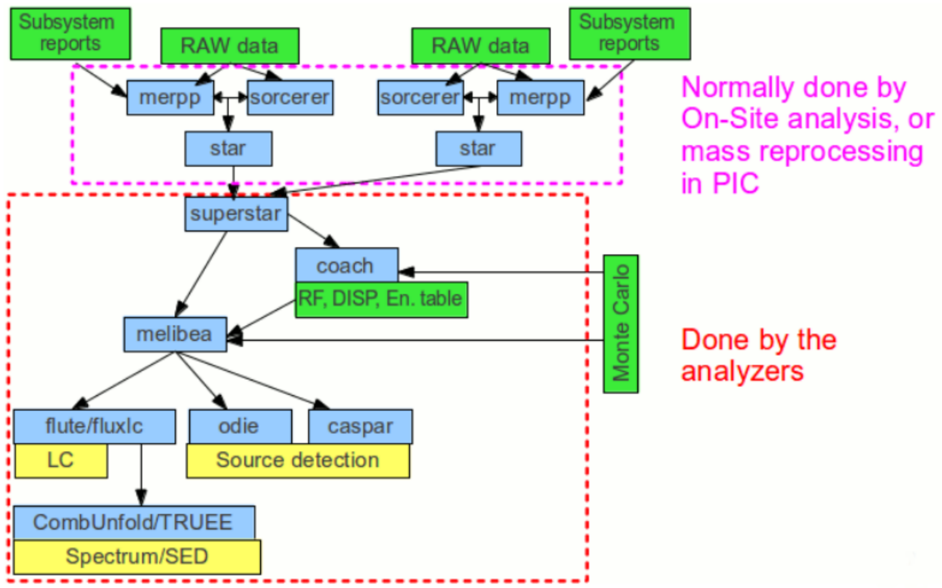

Figure 11: Standard MAGIC analysis scheme[6].

this purpose, data with the aerosol atmospheric transmission higher than 0.7 is taken and once again checked the zenith angle distribution of data which corresponded to 5° - 50° range. Data cuts can be, other than with `Quate`, made in different steps on `Melibea` (Merge and Link Image parameters Before Energy Analysis) or `Flute` (FLUx vs. Time and Energy) level later in the analysis.

In this case, reduction of the data time during the cuts was ~ 2 hours, so in conclusion, after the cuts 43.3 hours of data were left to continue the analysis with. Some of data was excluded due to inadequate zenith range, low light transmission and some due to bad weather conditions on the MAGIC site during the observations.

When data is selected and properly cut using `Quate`, next step is to perform the selection of γ rays in contrast to the background, most importantly showers of hadronic origin.

4.2.1 γ-ray selection - Random forest

The selection of γ-ray induced showers is done using sets of parameters that can distinguish them from showers of different origin. These parameters are strictly related to the development of the showers and to the image produced in the camera. For the separation between events of γ or hadron origin, there is an algorithm trained, called Random Forest (RF). Data used

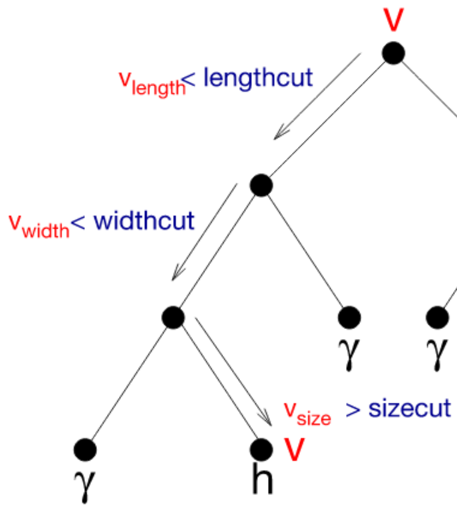

Figure 12: Random forest tree [55].

in RF training consists of OFF data with same specifications as initial data sample for main analysis (in e.g. zenith angle distribution) and Monte Carlo simulations of γ-ray showers. OFF data are chosen from the data set of the same observational nights, collected from points in the sky where number of γ-ray events is negligible. Data for Monte Carlo simulations for each observational period is available on MAGIC private grid for analyzers.
In summary, RF is produced as following: considering starting sample, first step is selecting random parameter. They are describing the shower and its image in the camera and one has parameters of different types in e.g. detector or observational parameters. Some of them can be mutually dependent, hence taken with care. Few most important parameters are width, length and size of the image in the camera. Next step is obtaining its optimal cut, given as a result of Gini index minimization. Gini index is defined as inequality of two distributions, where low Gini index corresponds to rather equal, while high Gini index corresponds to unequal distributions [55]. In each step, Gini index decrease is calculated for different cuts and chosen cut is the one with the maximal decrease. After the cut is carried out, what one gets are two samples, called branches, separated in the most optimal way possible considering that single parameter. Next steps include selecting other random parameters and repeating the procedure. Procedure is repeated iteratively until the final sample is consisted only of only gammas or hadrons. This final sample is called leaf. In Fig. 12, the structure of a RF tree is shown. All the parameters and cuts can be included in one parameter called hadroness.

Hadroness is a measure of the shower similarity to a typical shower of hadron origin. This parameter goes 0 - 1 with values close to 0 describing the γ-ray event, while hadron origin events have hadroness parameter in the whole range mentioned.
In MAGIC analysis, production of RF is carried out by applying the program `Coach` (Compressed Osteria Alias Computation of the Hadronness parameter) to the selected data. Application of hadroness parameter to the data is done using `Melibea` program, where every event gets assigned a particular value of the hadroness parameter. `Melibea` is an executable in `MARS` software in charge of applying results from `Coach` to the stereo parameter files from `Superstar`. Doing that, `Melibea` adds hadroness parameter and energy to each event. `Melibea` performs the energy and position reconstruction using a standard approach which is based on "look up tables".

4.2.2 High-level analysis

Programs considered as a part of the high level analysis are those providing the final scientific results, in contrast to previously discussed programs and executables who are "assembling data", applying cuts or reconstructing energy or position. Those programs are:

- `Odie`: creates θ^2 plots and calculates significance
- `Caspar`: produces skymaps
- `Flute`: provides flux calculation and as conclusion produces light curves, spectrum and SED
- `Fold` & `Combunfold`: unfolds the spectrum and provides the best fit to the data

`Odie` runs on `Melibea` data to produce θ^2 plots and calculate the significance of the data. θ^2 is the squared angular distance between the reconstructed and incident direction of the shower. The significance is calculated using Poisson statistics and likelihood ratio and exact formulas can be found in [56]. Generally it is expressed by number of Gaussian standard deviations, but it can also be expressed in terms of ON and OFF events. Number of ON events includes all the events recorded, while number of OFF events correspond to the number of background events. θ^2 histograms obtained with `Odie` are important for estimating these numbers which are essential in further flux calculation done by `Flute`. As of interpreting θ^2 plots, it is expected that the γ-ray events from the source will be reconstructed on the lower θ^2 values, while background events will be distributed equally over the whole θ^2 range. Next program used is `Caspar`. As mentioned, `Caspar` produces skymaps of the source in the field of view. A skymap is a two dimensional representation of the photons recorded by the camera, along with the assigned sky coordinates. In MAGIC, there are three types of coordinates used for production of skymaps: camera, azimuthal and equatorial coordinates, each assigned to data by `Melibea`. Important is to take into account that the data plotted is not direct, but rather reconstructed so errors are possible and actually expected. Using `Caspar` it is fairly easy to produce skymaps of the source, among all the output maps, information considering test statistics, significance and flux are provided. Most of the outputs can be easily interpreted but maybe most important here is the relative flux map, which shows ratio of numbers of excess and background events and it will be shown later (Fig. 22, and Fig. 23).

Flux calculations are performed by the program `Flute`. The needed ingredients are including number of γ-ray events, effective time and collection area. As mentioned for `Odie` case, the number of γ rays from the source (N_{Excess}), in case of point-like source, can be obtained from θ^2 plots. Events recorded, other than γ rays from the source, include also the background events within the same angular distance. Number N_{Excess} can be calculated using the formula:

$$N_{Excess} = N_{ON} - \alpha \times N_{OFF}, \tag{35}$$

On the θ^2 plot in the Fig. 13, one can see an example of strong signal from Crab Nebula observation, number of ON events is showed in red and represents all the events recorded, including signal and background. Black color shows OFF events representing background and as visible, their number is rather constant over the range of θ^2 values shown. Excess events in blue color are result of subtraction of OFF events from ON events and they represent signal, meaning γ rays. As it can be seen from the plot, higher number of γ-ray events are present on lower values of θ^2 which means in narrower cone around the pointing direction of the telescope. So in principle, in order to separate wanted data from the background, good background estimation is needed. For this reason, MAGIC telescopes are operating in wobble mode. Wobbling mode is defined as slight rotation of the source in the camera, with slight offset and defined wobble angle. For particular observations, more wobble positions can be used. Wobble mode ensures that while observing the source, also OFF data from nearby positions around the source is collected. In that way number of background events can be estimated. OFF positions are, same as in case of RF training, chosen from the points of the

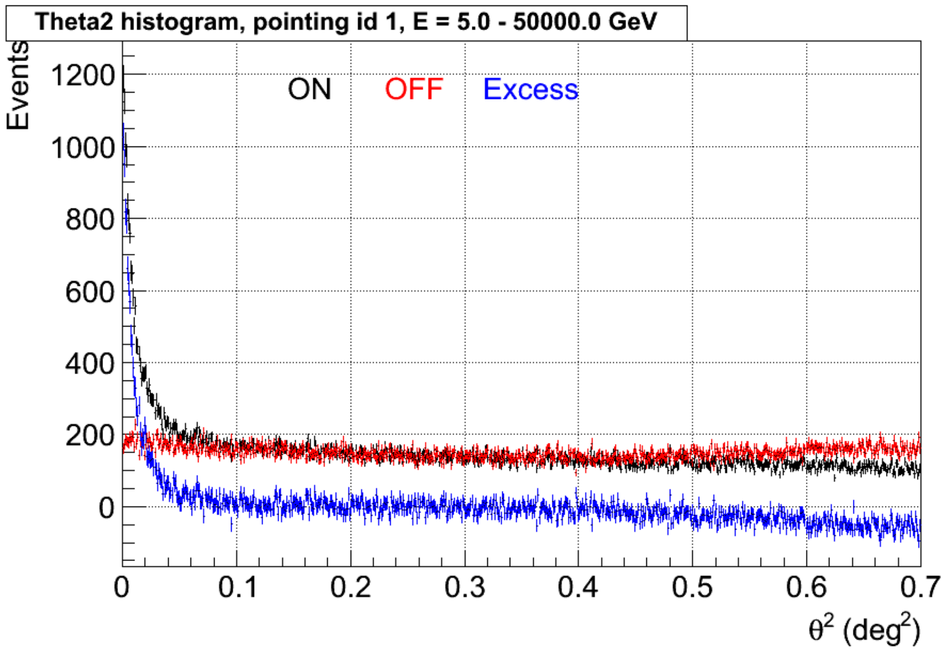

Figure 13: Crab Nebula θ^2 plot (from MAGIC Data analysis Manual).

sky where no γ-ray sources are present, also, on the same distance around the source. In this particular study, 2 pairs of wobble positions are used:

- W0.40+058 & W0.40+238
- W0.40+157 & W0.40+337

where 0.40 denotes θ^2 distribution from wobble offset of the Crab Nebula while second number is the wobble angle. Also, here used method of wobble observation was "OFF from wobble partner" shown in Fig. 14. This method is used because other than NGC 1275, another source, namely IC310, is present in the field of view which causes problems with standard wobbling in terms of acceptance in the field of view.
Second ingredient for the flux calculation is the effective time of observation. In general, this has to be considered since not all of the time elapsed during the observations is used for data taking. Main gaps between data taking time are caused by the dead time of the telescope and also ordinary gaps between data taking. Dead time of the telescope is time after recording an event in which telescope detector cannot acknowledge any new event. It can vary across the observational period because the readout upgrades of MAGIC and for this study is equal to 26 μs. Using dead time and ratio of true events, effective time is calculated from the elapsed time using an exponential fit to

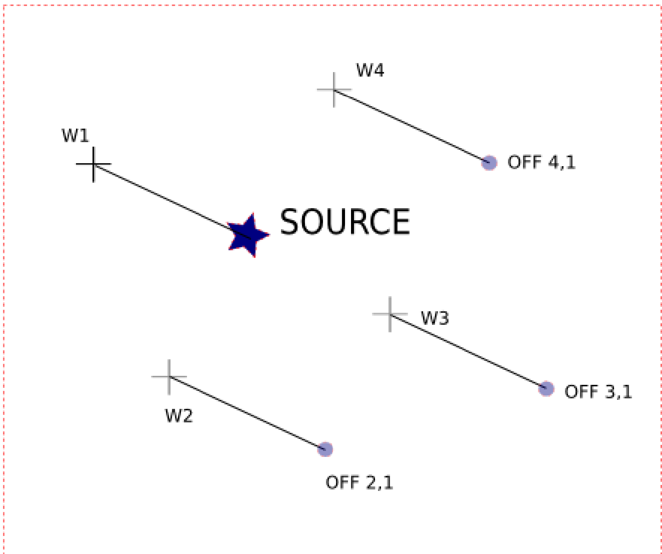

Figure 14: "OFF from the wobble partner" method (from MAGIC Data Analysis Manual).

the distribution.
Last part needed is the effective collection area. Effective collection area is defined as area of an ideal detector that detects the same rate of γ rays as MAGIC detector does. It depends on multiple factors: zenith angle, energy of the incident particle, angle between the pointing direction of the telescope and direction of the γ ray. Some of these dependencies are taken into account in MAGIC software and can be easily estimated, while others can be calculated using the Monte Carlo simulations.
When all the ingredients are obtained, γ-ray flux can be calculated using the equation:

$$\Phi = \frac{d^2 N_\gamma}{dSdt} \tag{36}$$

with units of $[L^{-2}][t^{-1}]$. Evolution of the γ-ray flux in time is represented by a light curve and the one obtained in this work will be, along with other results, shown later in Fig. 26. One can also obtain differential energy spectrum, which is the flux per energy interval:

$$\frac{d\Phi}{dE} = \frac{d^3 N_\gamma}{dSdtdE} \tag{37}$$

Its units are $[L^{-2}][t^{-1}][E^{-1}]$. Most commonly used output of `Flute` is the SED which is the differential energy spectrum multiplied with the squared energy:

$$E^2 \frac{d\Phi}{dE} \tag{38}$$

Multiplication with energy is needed for easier comparison with results from other sources because SED shows exactly how much energy each source is emitting. In order to complete the analysis, the spectrum has to be further "processed". The energy estimated up to the `Flute` analysis level has a finite resolution and the measurement is also affected by a limited acceptance. Also, reconstructed energy is dependent on the parameters of the image, impact parameter and others. These parameters further on, effect the estimated energy and limit its resolution. For this reason, unfolding procedures are used to obtain the estimators of the true energy spectrum of the source.

4.2.3 Unfolding

The unfolding of the MAGIC spectrum provides the analyzers with the true energy of the source, rather than the one estimated which is obtained from `Flute`. As indicated[7], the energy estimation for IACTs suffers of several problems. First, since the energy of the γ-ray events is reconstructed from the image of the Cherenkov light in the camera produced by the shower, one is dealing with an indirect measurement, dependent on reconstruction methods and Monte Carlo simulations. Secondly, not all of the γ rays from the part of sky observed will be detected: the acceptance of the detector is limited and energy-dependent, due to the event selection at trigger level and at later stages in the analysis chain. A third problem is given by the statistical uncertainties, which in MAGIC are energy-dependent and around the 15 %.

In MAGIC and in this work, two executables from `MARS` are used, involving several different models and fits to the spectra. The first unfolding executable is `Fold`. `Fold` is using the forward folding Poisson likelihood maximization. This unfolding procedure assumes a fit to the spectrum obtained with `Flute`. This approach is useful when the function that describes the spectrum is known and the only thing missing are the best parameters of the fit. Functions available for fitting, and used in this work are power-law (PWL), log-parabola (LP), power-law with exponential cut-off (EPWL) and log-parabola with exponential cut-off (ELP). `Fold` works on the output file obtained by `Flute`. The output of `Fold` includes parameters of the fit and their uncertainties. Usually, `Fold` is also useful when one wants to compare

[7] https://www.desy.de/ blobel/eBuch.pdf

different fits to the same spectrum.
The other unfolding executable is `Combunfold`. It involves several regularization methods that can be applied, and also one regularization method including the iteration. Many different algorithms can be used for the unfolding, and the stability of spectrum under all of them can be tested (see Fig. 30).

4.3 Modelling of photon-ALP oscillations in galaxy cluster enviroment

In order to calculate the predictions of effects photon-ALP oscillation on the AGN spectrum, in this case NGC 1275 in center of the Perseus galaxy cluster, one needs to solve equations of motion of the system involved. To begin with the description of the process, first part is the Lagrangian of the photon-ALP system:

$$\mathcal{L} = \mathcal{L}_{a\gamma\gamma} + \mathcal{L}_{EH} + \mathcal{L}_a. \tag{39}$$

Here included are the term explaining photon-ALP coupling $\mathcal{L}_{a\gamma\gamma}$, already written before (Eq. 30), $\mathcal{L}_{EH}$ which represents effective Euler-Heisenberg Lagrangian for corrections of QED loops in photon propagators due to an external magnetic field [57] and the last term $\mathcal{L}_a$ which is describing the kinetic and mass term of axionic field. The full Lagrangian can be written:

$$\mathcal{L} = -\frac{g_{a\gamma\gamma}}{4} F_{\mu\nu} \tilde{F}_{\mu\nu}\, a + \frac{\alpha^2}{90\, m_e^4} \left[(F_{\mu\nu} F^{\mu\nu})^2 + \frac{7}{4} (F_{\mu\nu} \tilde{F}_{\mu\nu})^2 \right] + \frac{1}{2} (\partial_\mu a\, \partial^\mu a - m_a^2\, a^2). \tag{40}$$

As in previous studies [7, 2], the photon beam moving in the x_3 direction, is observed. Generally, for a polarized photons and relativistic ALPs, equations of motion become:

$$\left(i \frac{d}{dx_3} + E + \mathcal{M} \right) \begin{pmatrix} A_1(x_3) \\ A_2(x_3) \\ a(x_3) \end{pmatrix} = 0. \tag{41}$$

Here, $\mathcal{M}$ is the photon-ALP mixing matrix, while $A_1(x_3)$ and $A_2(x_3)$ represent photon linear polarization amplitudes along the x_1 and x_3 axis, respectively, and $a(x_3)$ is the axion field strength [7]. Solution of this equation is transfer function $\mathcal{T}(x_3, 0; E)$ using the condition $\mathcal{T}(0, 0; E) = 1$. Photon beam propagating in cold and ionized plasma is assumed. In this case also an homogeneous magnetic field is assumed, transverse to propagation direction of the photon beam, and laying in x_2 direction. Then mixing matrix can be simplified to:

$$\mathcal{M}_0 = \begin{pmatrix} \Delta_\perp & 0 & 0 \\ 0 & \Delta_\parallel & \Delta_{a\gamma} \\ 0 & \Delta_{a\gamma} & \Delta_a \end{pmatrix}. \tag{42}$$

Elements in this matrix are taking in account plasma effects, QED vacuum birefringence effect, axion field and photon-ALP mixing. Namely they can be written as:

$$\Delta_a = -\frac{m_a^2}{2E}$$
$$\Delta_\parallel = \Delta_{pl} + \frac{7}{2}\Delta_{QED}$$

and

$$\Delta_\perp = \Delta_{pl} + 2\Delta_{QED},$$

where

$$\Delta_{pl} = -\frac{\omega_{pl}}{2E} \quad \text{and} \quad \Delta_{QED} = \frac{\alpha E B^2}{4\pi B_{CR}^2}.$$

Here, B_{CR} is critical magnetic field $B_{CR} \sim 4.4 \times 10^{13}$G, α the fine structure constant and ω_{pl} is the plasma frequency, connected to the ambient thermal electron density. The last term, as mentioned, represents photon-ALP mixing:

$$\Delta_{a\gamma} = \frac{1}{2} g_{a\gamma\gamma} B_\perp. \tag{43}$$

As previously noted, magnetic field transverse to the propagation direction of the photon beam is supposed. That means that the photon-ALP mixing is induced by that component and as seen in Eq. 36, it presents an off-diagonal term. Since here the units of introduced components will not be evaluated, they can be read from [25, 58]:

$$\Delta_a \simeq -7.8 \times 10^{-3} \left(\frac{m_a}{10^{-8}\ \text{TeV}}\right)^2 \left(\frac{E}{\text{eV}}\right)^{-1} \text{kpc}^{-1}$$
$$\Delta_{pl} \simeq -1.1 \times 10^{-10} \left(\frac{n_e}{10^{-3}\ \text{cm}^{-3}}\right) \left(\frac{E}{\text{TeV}}\right)^{-1} \text{kpc}^{-1}$$
$$\Delta_{QED} \simeq 4.1 \times 10^{-6} \left(\frac{B_\perp}{10^{-6}\ \text{G}}\right)^2 \left(\frac{E}{\text{TeV}}\right) \text{kpc}^{-1}$$
$$\Delta_{a\gamma} \simeq 7.6 \times 10^{-2} \left(\frac{g_{a\gamma\gamma}}{5 \times 10^{-11}\ \text{GeV}^{-1}}\right) \left(\frac{B_\perp}{10^{-6}\text{G}}\right) \text{kpc}^{-1}$$

When taken into account that VHE γ rays are considered, effect of the vacuum birefringence can be neglected. Another important thing that still was not mentioned here is the photon absorption. In this case the absorption of the EBL is neglected, but in case it is not negligible, $\Delta_{\parallel}$ and $\Delta_{\perp}$ have to be modified.
Generally magnetic field B doesn't have to be in x_2 direction, but it can generate an angle ψ with it. That situation demands a different approach, meaning that the angle ψ has to be included in form of similarity transformation. That ultimately gives the new form of solution to the equations of motion:

$$\mathcal{T}(x_3, 0, E; \psi) = V(\psi)\, \mathcal{T}(x_3, 0, E) \times V^{\dagger}(\psi), \tag{44}$$

and $\mathcal{M}$ is changed in:

$$\mathcal{M} = V(\psi)\, \mathcal{M}_0\, V^{\dagger}(\psi) \tag{45}$$

To further include the magnetic field in this study, its morphology will have to be assumed. To begin with, take one magnetic domain of length d with constant magnetic field. Taking this, calculated probability of photon-ALP oscillation [57] is:

$$\begin{aligned} P_{\gamma\to a} &= (\Delta_{a\gamma}\, d)^2 \frac{\sin^2(\Delta_{\mathrm{osc}}\, d/2)}{(\Delta_{\mathrm{osc}}\, d/2)^2} \\ &= \sin^2 2\theta \sin^2\left(\frac{\Delta_{\mathrm{osc}} d}{2}\right), \end{aligned} \tag{46}$$

where θ is rotation angle:

$$\theta = \frac{1}{2} arcsin\left(\frac{2\Delta a d}{\Delta_{osc}}\right). \tag{47}$$

Here, the Δ_{osc} is oscillations wave number given by:

$$\Delta_{osc}^2 = [(\Delta_a - \Delta_{pl})^2 + 4\Delta_{a\gamma}^2]. \tag{48}$$

This term can also be written in terms of critical energy E_{crit}, that is obtained when neglecting birefringence effects, from Eq. 32 [32]:

$$\Delta_{osc} = 2\Delta_{a\gamma}\sqrt{1 + \left(\frac{E_c}{E}\right)^2} \tag{49}$$

Due to the fact that unpolarized photons have to be investigated, since so far, polarisation of VHE γ rays is not measured, solving the equation of motion has to be reformulated in sense of density matrices [7]. Then the equation of motion becomes:

$$i\,\frac{d\rho}{dx_3} = [\rho, \mathcal{M}_0], \tag{50}$$

where ρ is density matrix, generally written as [7]:

$$\rho\left(x_3\right) = \begin{pmatrix} A_1\left(x_3\right) \\ A_2\left(x_3\right) \\ a\left(x_3\right) \end{pmatrix} \otimes \left(A_1\left(x_3\right)\ A_2\left(x_3\right)\ a\left(x_3\right)\right)^*. \tag{51}$$

Solution of (38) is given with [59]:

$$\rho\left(x_3\right) = \mathcal{T}\left(x_3, 0; E\right)\rho(0)\mathcal{T}^\dagger\left(x_3, 0; E\right). \tag{52}$$

In previous discussion, homogeneous magnetic field with single domain in which B is constant was assumed. In reality what is needed is to divide it in N different domains. By doing this, transfer matrix is changed :

$$\mathcal{T}\left(x_{3,N}, x_{3,1}; \psi_N, \ldots, \psi_1; E\right) = \prod_{i=1}^{N}\mathcal{T}\left(x_{3,i+1}, x_{3,i}; \psi_i; E\right), \tag{53}$$

and complete photon survival probability $P_{\gamma\gamma}$ after it is passed through N domains is [60]:

$$P_{\gamma\gamma} = \sum_{j=1,2}\operatorname{Tr}\left(\rho_{jj}\mathcal{T}\rho_0\mathcal{T}^\dagger\right), \tag{54}$$

where $\rho_{jj} = \mathrm{diag}(\delta_{1j}, \delta_{2,j}, 0)$ is the polarisation of the photon. From considering all of the domains, as calculated in [61] averaged photon survival probability is:

$$P_{\gamma\gamma} = \frac{1}{3}\left(1 - \exp\left(-\frac{3}{2}\Delta_{a\gamma}^2 r L_{\mathrm{coh}}\right)\right), \tag{55}$$

where r is the propagation distance and L_{coh} is coherent length of domains through which photon-ALP beam is propagating.

4.3.1 GammaALPs code

Modelling of photon-ALP oscillations in this work is performed using the python code GammaALPs[8]. GammaAPLs is a public code that calculates $P_{\gamma\gamma}$. $P_{\gamma\gamma}$ is defined as probability that from initially unpolarized photon, polarized γ ray will be detected. GammaALPs solves equations of motion for the photon-ALP system using the transfer matrix method. Considering

[8]https://github.com/me-manu/gammaALPs

Parameter	Value
σ_B	10 μG
η	0.5
r_{max}	500 kpc
q	-2.8
K_L	0.18 kpc^{-1}
K_H	9 kpc^{-1}

Table 1: Parameters of magnetic field used in this study.

other effects that could impact the photon flux, GammaALPs includes the EBL absorption [27], dissipation in QED and CMB effects. In this particular case, the above mentioned procedure is followed and $P_{\gamma\gamma}$ is calculated in the magnetic field of the Perseus galaxy cluster along with the possible conversion in the Milky Way magnetic field. Oscillations in the intergalactic magnetic field are neglected due to very low upper limits ($\lesssim 10^{-9}$G) on the strength of the magnetic field. With this strength of magnetic field, constraints on the masses of ALPs and their coupling with photons have already been set [62, 63], so in this case, with low redshift, oscillations in intergalactic magnetic field can be neglected. Model used to describe the intra-cluster magnetic field can be found in [64]. This model uses Gaussian turbulence to model the transverse components of a turbulent magnetic field with zero mean and variance σ_B. Since it is suggested that the magnetic field in the cluster depends on the electron density of the intra-cluster medium given by the $B(r) = B_0(n_e(r)/n_e(r = 0))^\eta$, parameters and electron density η are needed and taken from [65]. Also, turbulence scales K_L, K_H and turbulence spectral index q for magnetic field are taken from [66]. Table 1 below shows the parameters taken in the calculation with GammaALPs. Here r_{max} is the cluster extension, meaning the distance beyond which magnetic field of cluster is negligible.
Second environment considered having magnetic field is our galaxy, Milky Way. Modelling of Milky Way used in GammaALPs code is based on the model from [67], made by combining results from rotation measurements and polarized synchrotron radiation. Also, EBL absorption is taken following [27]. In this work of thesis, a study of the ALPs parameters space has been performed. This study was made in order to obtain a better insight in the behaviour and dependence of the $P_{\gamma\gamma}$ on different values of ALPs mass m_a and coupling to photons g_{11}. GammaALPs calculates $P_{\gamma\gamma}$ for 10 different realizations of magnetic field and in this thesis, averaged value over all realizations will be considered.

4.3.2 Study of ALPs parameter space

Goal is to "fold" a MAGIC spectrum without ALPs contribution with the GammaALPs predictions and then perform a comparison of the convolution with the spectrum and search for matches. This is done by calculating the sums of squared residuals and comparing them among different parameters sets. For the convolution between the MAGIC spectrum without ALPs and the $P_{\gamma\gamma}$, to represent the spectrum without ALPs, a fit to the MAGIC spectrum, a general function (EPWL) that approximates the spectrum but not so precisely to be able to appreciate the tiny wiggles which are signatures of ALPs is used. Then it is folded with $P_{\gamma\gamma}$ and the convolution function which carries the ALPs prediction and can be compared to the intrinsic spectrum is obtained. This procedure is inspired by [2], in which the search for ALPs signatures was conducted for averaged *Fermi*-LAT data. Ultimately, the best way to perform this comparison would be using a likelihood function as it was done in [2], but for now, scope of this work will include checking which part of ALPs parameters space would lead to results that could possibly explain the reduction of the flux in the AGN spectra considered. This will be further revised in a later study. For purposes of this work, approximate values of parameters of ALPs are needed. Different values of m_a and g_{11} will be addressed. In earlier articles using data from MAGIC and *Fermi*-LAT [28, 8], a part of ALPs parameter space around $m_a \sim 100$ neV and $g_{11} \sim 1$ was considered. In this work the parameter space around these values is probed. As seen in Fig. 15, for current VHE and HE γ-ray experiments, certain part of ALP parameter space is available for probing, so boundary values probed are inside the blue rectangle. In the present work, sets of parameters which can produce oscillations in the energy range of MAGIC spectrum of NGC 1275 are selected. Then the oscillations predicted are folded to a simple fit to the spectrum, and the "predicted" spectrum is then compared with the intrinsic MAGIC spectrum, searching for matches and signatures of ALPs oscillations. The comparison is performed by calculating and comparing the sums of squared residuals.

The first step of this study was to plot the $P_{\gamma\gamma}$ for sets of parameters reasonable, considering previous studies [28, 8]: Observing the oscillations in Fig. 16, it was decided to exclude the lowest value of the coupling since no significant oscillations are produced. With the opposite reason, also the highest value of coupling is excluded. Next step of this study was to examine $P_{\gamma\gamma}$ in a narrower range of parameters, including only coupling g_{11} of 0.3 and 0.5 but still probing different masses, in the range of 90 neV - 110 neV. Results

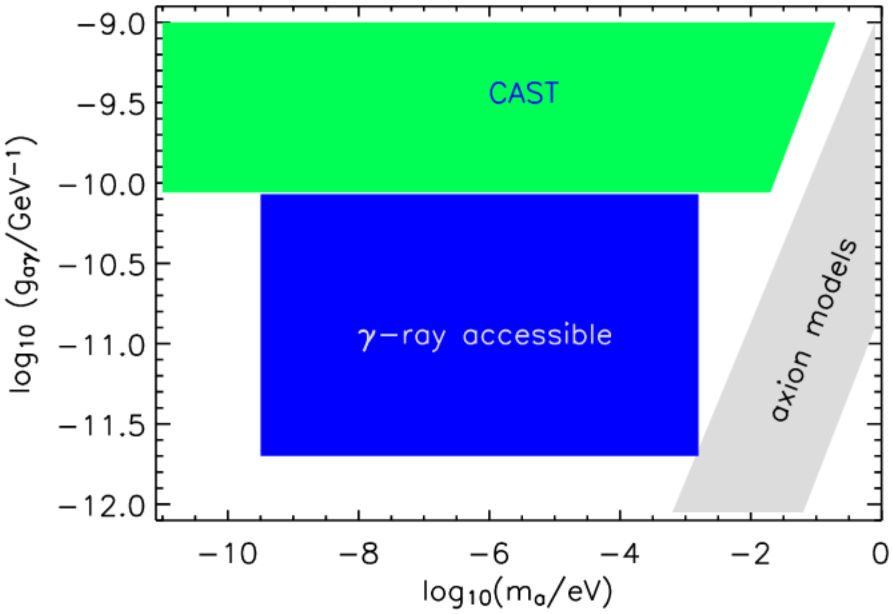

Figure 15: Part of parameter space available for probing with γ-ray experiments [28].

are shown in Fig. 17.

The goal of this study was to examine $P_{\gamma\gamma}$ for different combinations of photon-ALP coupling and ALP mass values to continue with comparing the fit of the SED folded with the prediction and intrinsic SED. Folding with the prediction was done simply by producing the convolution of the fit of the spectrum and interpolation of the $P_{\gamma\gamma}$ for the chosen set of parameters. The final comparison of the convolution with the intrinsic SED would be to calculate the likelihood which is above the scope of this work. In that way, one would obtain the most promising parameters of ALPs that could be accounted for causing irregularities in the spectrum and if not detect, possibly put constraints on part of the ALPs parameter space. For now, comparison was done by calculating the sums of squared residuals and comparing them in order to find the set with the lowest value of squared residuals sum. This was done using sets of parameters from Fig. 17 and the results will be presented in Sec. 5.

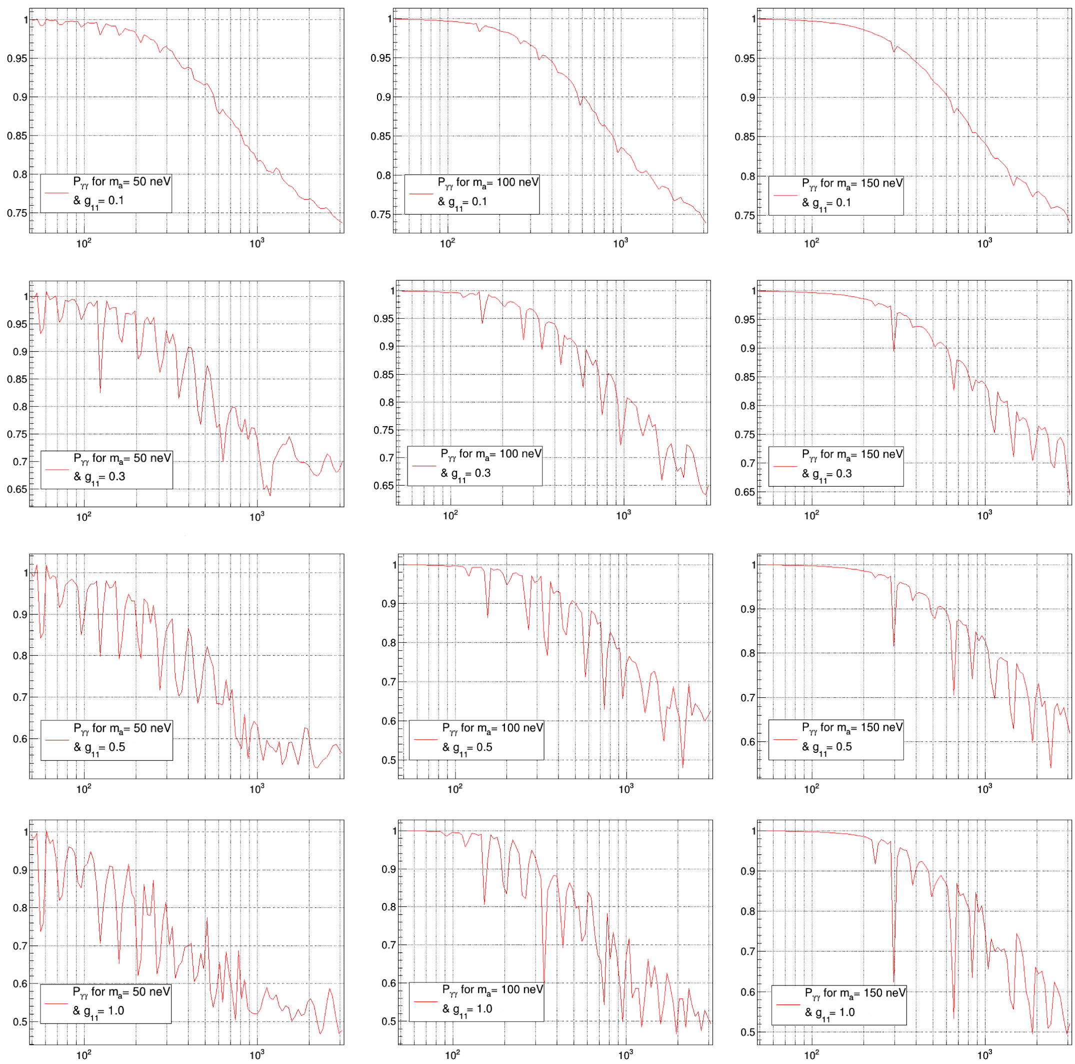

Figure 16: Study of ALPs parameter space, Part 1.

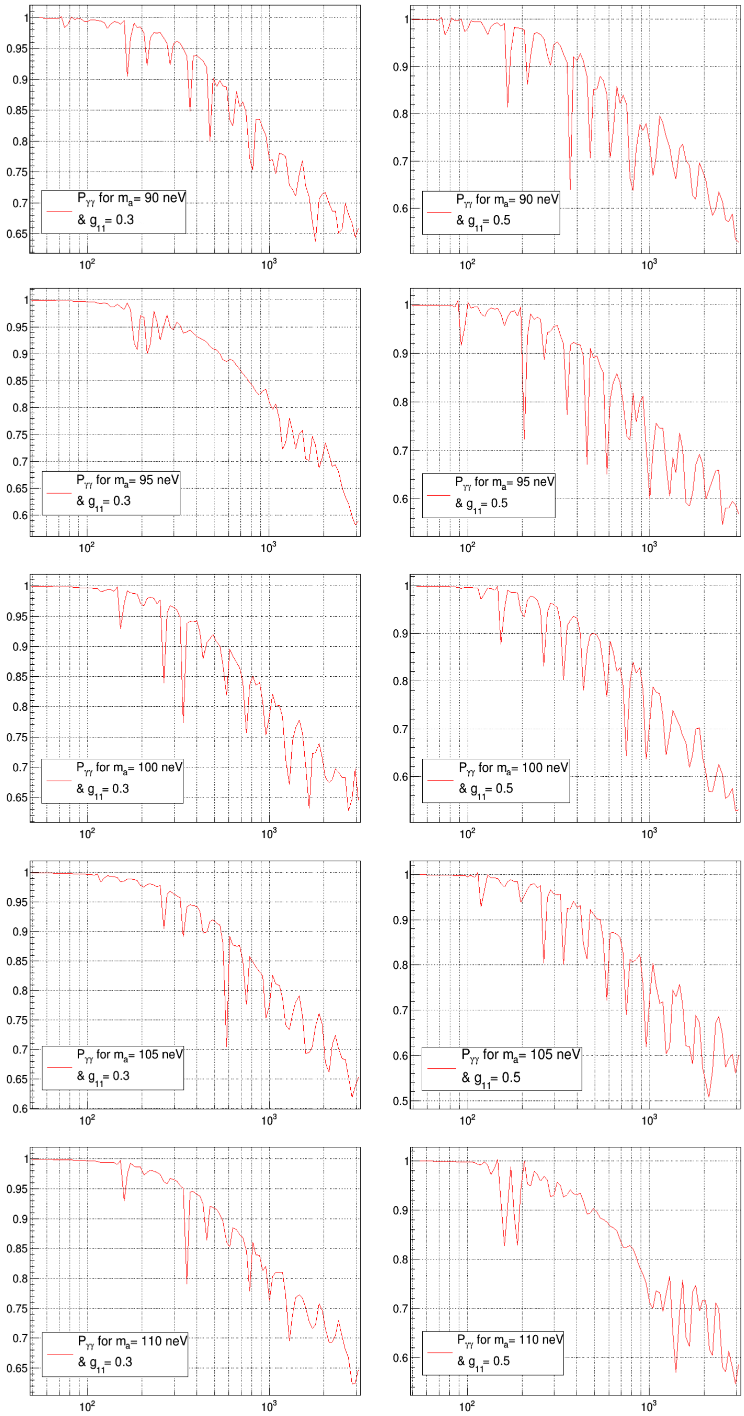

Figure 17: Study of ALPs parameter space, Part 2.

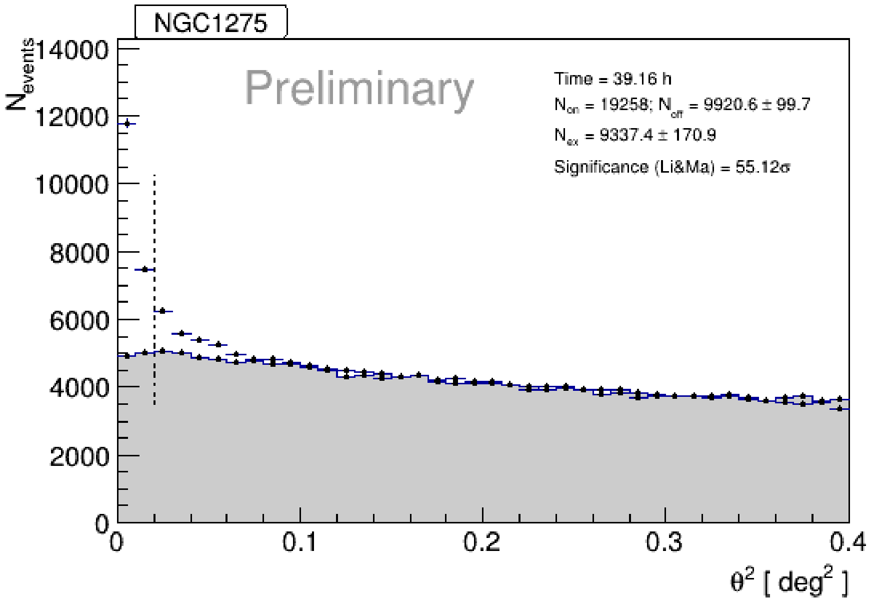

Figure 18: θ^2 plot of ST_03_07 for low energy range cuts.

5 Results and discussion

The first part of the data analysis consisted in creating the RF from OFF data and MCs simulations, and cleaning the data by applying quality cuts. After that, `Odie` program was used in order to obtain significance maps for the data from observational period ST_03_07. In `Odie` different standard cuts based on the energy and other parameters of the shower can be applied. They are low energy cuts ($\sim$ 100 GeV), full range cuts ($>$250 GeV) and high energy cuts ($>$1 TeV). From Fig. 18 and Fig. 19 one can observe that the significance for the whole sample (39.2 hours) is 35.9 σ for the full energy cuts and 47.5 σ for the low energy range cuts. This is a considerably high significance, considering that the minimum significance necessary for claiming a detection is 5 σ. In order to study daily significance,production of θ^2 plots is repeated for each day separately. Results are shown in Tab. 2. As observed, the night with the highest significance is 01 Jan 2017. This is a very bright flare and it is used in this study of ALPs signatures. The motivation is that a bright flare with an high number of events can give us more resolution of the spectrum in the search of tiny wiggles predicted in case of ALPs. Also the short time of the observation can favour the search for oscillations rather than a long term spectrum obtained averaging several nights of observations.

One should be aware that another approach could be used, gathering high

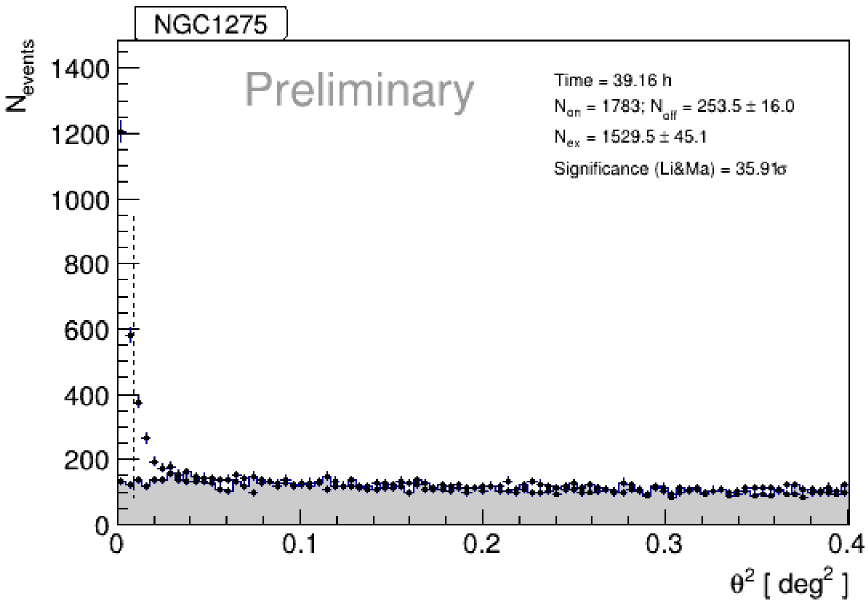

Figure 19: θ^2 plot of ST_03_07 for full energy range cuts.

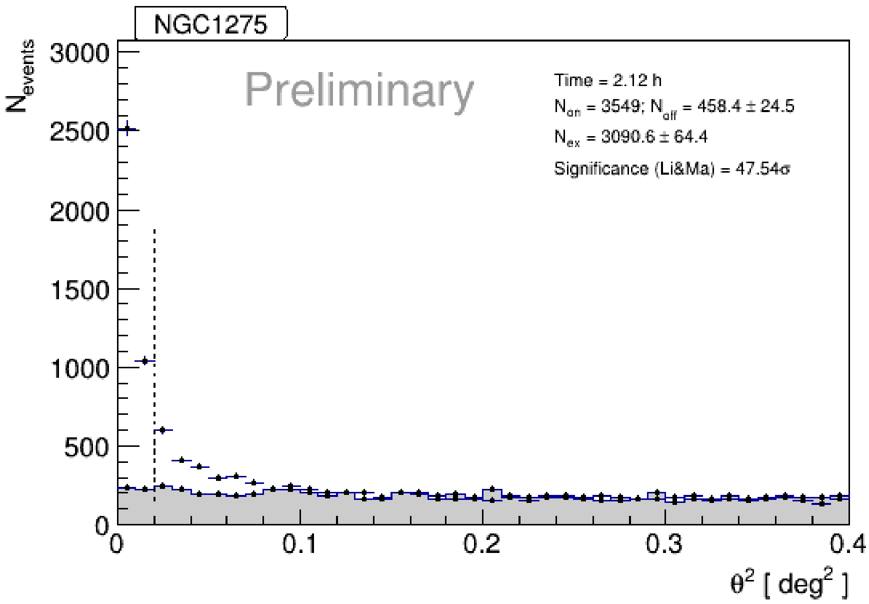

Figure 20: θ^2 plot of 01 Jan 2017 for low energy range cuts.

DAY	t_{eff} / h	Full range (σ)	Low energy (σ)
2016_09_10	0.9	2.3	1.0
2016_10_01	1.0	-0.5	-1.8
2016_10_10	1.1	2.0	0.6
2016_10_29	3.4	6.7	9.0
2016_10_30	3.	12.	21.6
2016_10_31	3.1	5.0	11.7
2016_10_01	1.9	2.1	1.3
2016_11_02	2.6	7.3	11.2
2016_11_07	2.6	2.7	7.5
2016_11_08	2.4	4.0	6.8
2016_11_27	0.9	2.0	1.4
2016_12_06	2.7	2.2	3.7
2016_12_07	0.8	2.9	3.4
2016_12_28	1.3	4.5	9.0
2017_01_01	2.1	25.3	47.5
2017_01_03	2.4	17.4	31.6
2017_01_04	2.6	12.6	17.0
2017_01_18	0.9	-0.3	0.1
2017_01_26	0.8	1.0	0.5
2017_01_30	0.9	-0.1	1.3
2017_02_17	1.0	0.8	2.0

Table 2: Daily significances from ST_03_07.

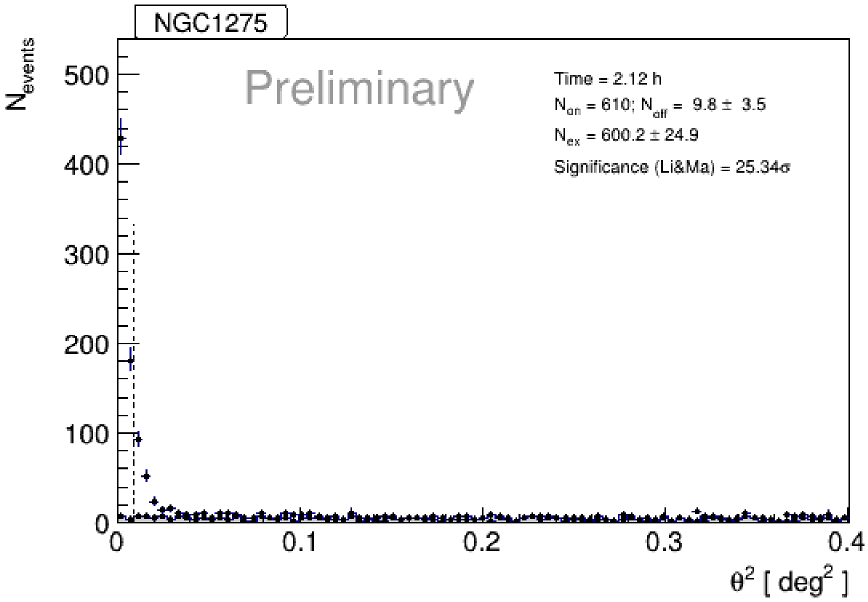

Figure 21: θ^2 plot of 01 Jan 2017 for full energy range cuts.

statistics with the use of more observational periods, but the latter one would be a longer time study which would imply the analysis of a huge set of data.

Moreover one cannot be sure that an averaged spectrum could be the best option, because of the known variability of the source. The θ^2 plots for the flaring night, obtained using low energy and full range `Odie` cuts respectively, are shown in Fig. 20 and Fig. 21.

`Caspar` was used to produce skymaps shown in the figures, both for the whole observational period and flaring day separately. One particular night (03 Sep 2016) showed misalignment of the skymap with pointing direction of the telescope. Relative flux plots from `Caspar` for ST_03_07, obtained with both low and full energy range cuts are shown in Fig. 22 in right and left panel respectively. The source was successfully localized and detected with high significance of the signal, which is visible from the color scale on the right side of plot which indicates bigger significance as color gets brighter. Since the flaring state of this source is a part of interest of this study, Sky maps produced for the flaring day only (01 Jan 2017) were also produced in Fig. 23 we show the one obtained by low energy cuts with `Caspar`.

According to the results from `Odie`, but also in the skymaps, is possible to see that the source was detected with high significance (>16 σ).

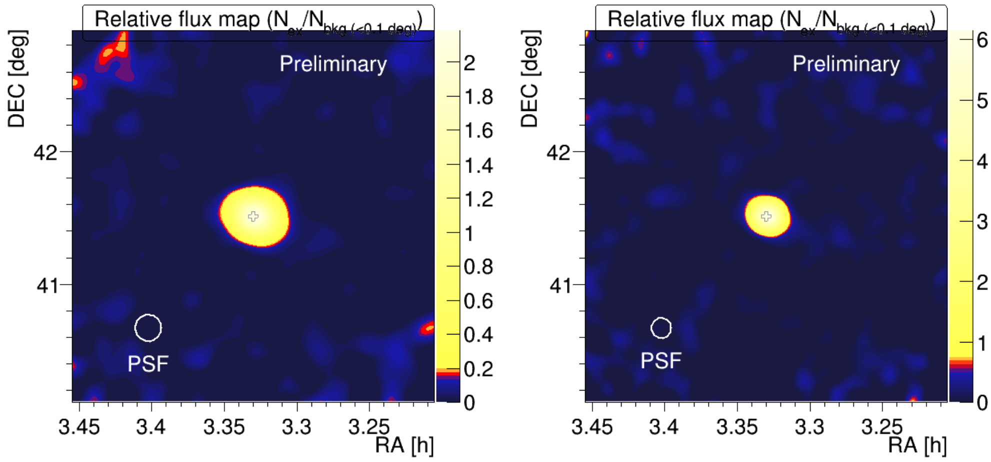

Figure 22: Relative flux maps of NGC 1275 for ST_03_07 obtained by `Caspar` with low energy range cuts (left) and full range cuts (right).

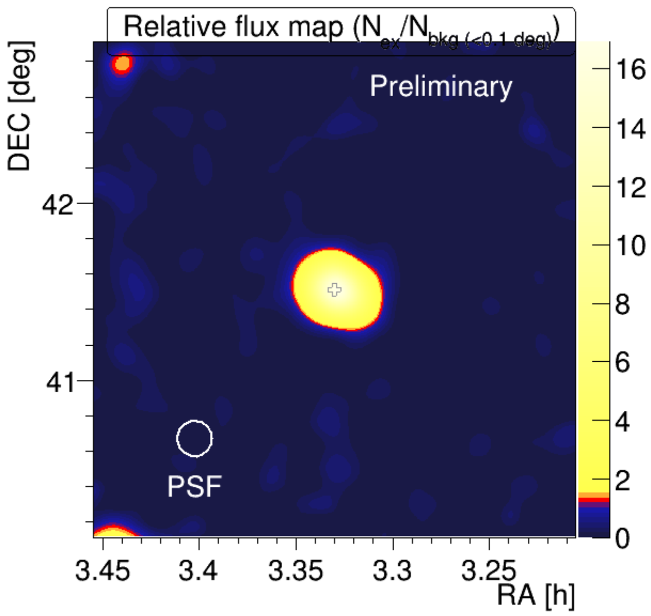

Figure 23: Relative flux map of NGC 1275 for flaring day (01 Jan 2017) obtained with low energy cuts.

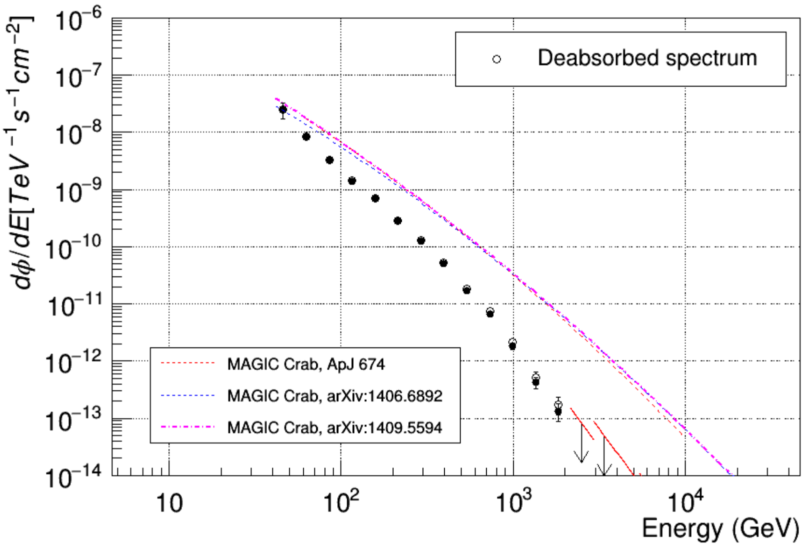

Figure 24: Spectrum of NGC 1275 from ST_03_07.

Flux calculations are performed by `Flute`, both for the whole sample of nights in ST_03_07 and for the flaring night 01 Jan 2017 only. The obtained spectrum and SED from ST_03_07 are shown in Fig. 24 and in Fig. 25 respectively.

The SED is not well described by a PWL function (see Table 4). This is promising since this work is based on looking for oscillations and wiggles as signatures from the ALPs interactions. The energy range of both spectrum and SED is in the range ~ 50 GeV $-$ 1000 GeV. In order to get the fluxes for each of the nights of the observational period, a light curve is produced and shown in Fig. 26.

The light curve shows significant activity of NGC 1275 in the observed period, as expected.

Fluxes and their upper limits, in case they exits, of all the nights in the sample are listed in Tab. 3.

As it can be seen from Tab. 3, the highest flux is obtained in date 01 Jan 2017, as expected. In order to proceed with the analysis it is decided to differentiate three different states of the source, using the light curve in Fig. 26. Nights with total flux $< 1\times10^{-10}$ are sampled as "low activity" state. Days with $1\times10^{-10} <$ flux $< 5\times10^{-10}$ are sampled as "active" state, while the night with highest flux was named the "flaring" state. It was decided to proceed with the analysis of the flaring state, since its flux is the highest, it has the highest signal to noise ratio, highest significance and telescope conditions don't vary much due to the fact that those events were

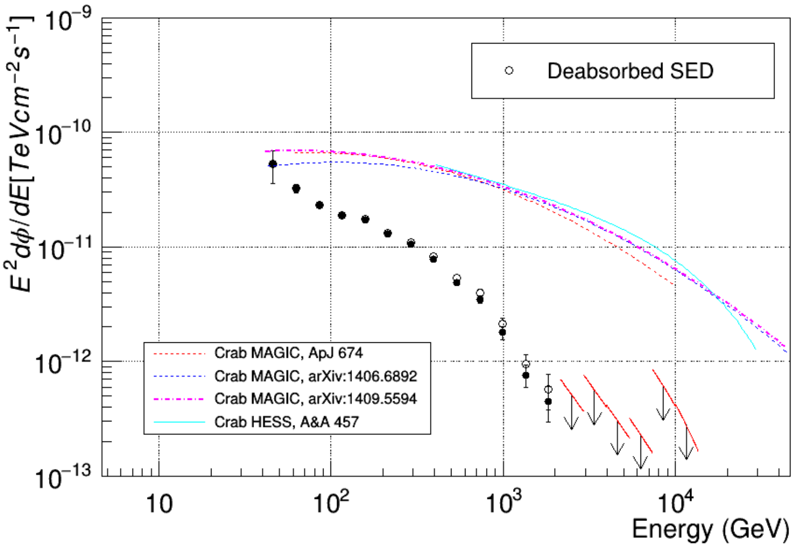

Figure 25: SED of NGC 1275 from ST_03_07.

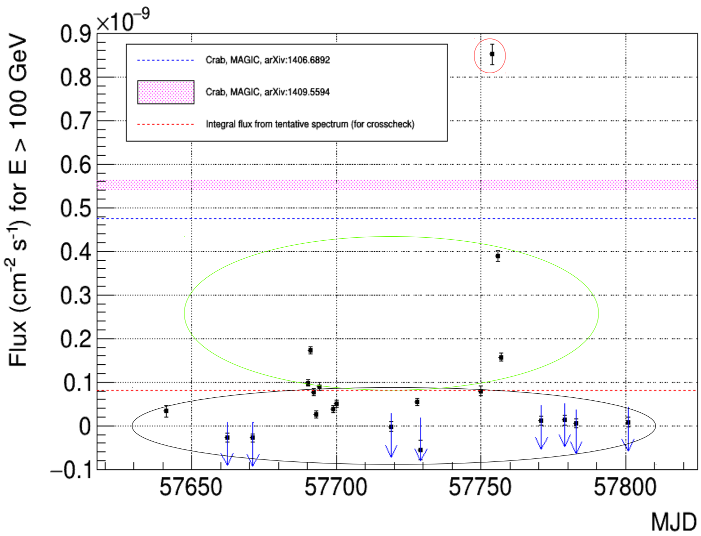

Figure 26: Light curve of NGC 1275 from ST_03_07.

DAY	Flux/$cm^{-2}s^{-1}$	Error/$cm^{-2}s^{-1}$	Upper limit
2016_09_10	3.4×10^{-11}	1.3×10^{-11}	-
2016_10_01	-2.7×10^{-11}	1.0×10^{-11}	8.6×10^{-12}
2016_10_10	-2.7×10^{-11}	9.1×10^{-12}	6.9×10^{-12}
2016_10_29	9.9×10^{-11}	7.8×10^{-12}	-
2016_10_30	1.7×10^{-10}	8.4×10^{-12}	-
2016_10_31	7.7×10^{-11}	7.4×10^{-12}	-
2016_10_01	2.7×10^{-11}	8.0×10^{-12}	-
2016_11_02	9.1×10^{-11}	8.3×10^{-12}	-
2016_11_07	3.8×10^{-11}	7.5×10^{-12}	-
2016_11_08	5.1×10^{-11}	7.9×10^{-12}	-
2016_11_27	-1.4×10^{-12}	1.2×10^{-11}	2.8×10^{-11}
2016_12_06	5.4×10^{-11}	8.4×10^{-11}	-
2016_12_07	-5.5×10^{-11}	2.2×10^{-11}	1.9×10^{-11}
2016_12_28	8.0×10^{-11}	1.1×10^{-11}	-
2017_01_01	8.5×10^{-10}	2.4×10^{-11}	-
2017_01_03	3.9×10^{-10}	1.3×10^{-11}	-
2017_01_04	1.6×10^{-10}	9.2×10^{-12}	-
2017_01_18	1.2×10^{-11}	1.0×10^{-11}	4.6×10^{-11}
2017_01_26	1.3×10^{-11}	1.2×10^{-10}	5.1×10^{-11}
2017_01_30	5.5×10^{-12}	1.1×10^{-11}	3.6×10^{-11}
2017_02_17	8.8×10^{-12}	1.1×10^{-11}	4.2×10^{-11}

Table 3: Daily fluxes from ST_03_07.

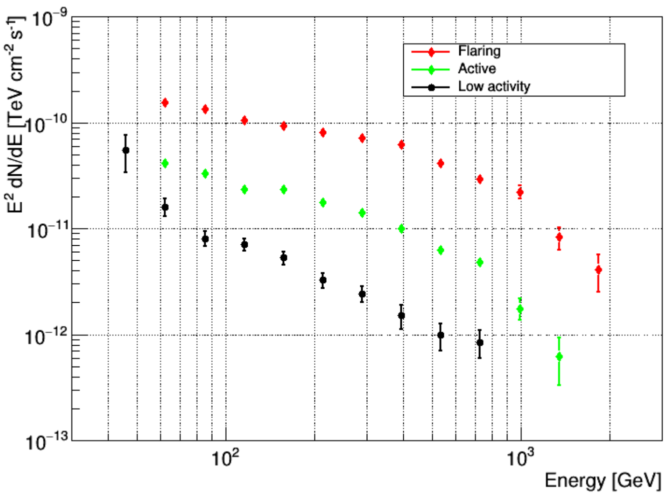

Figure 27: SED for three different states of NGC1275.

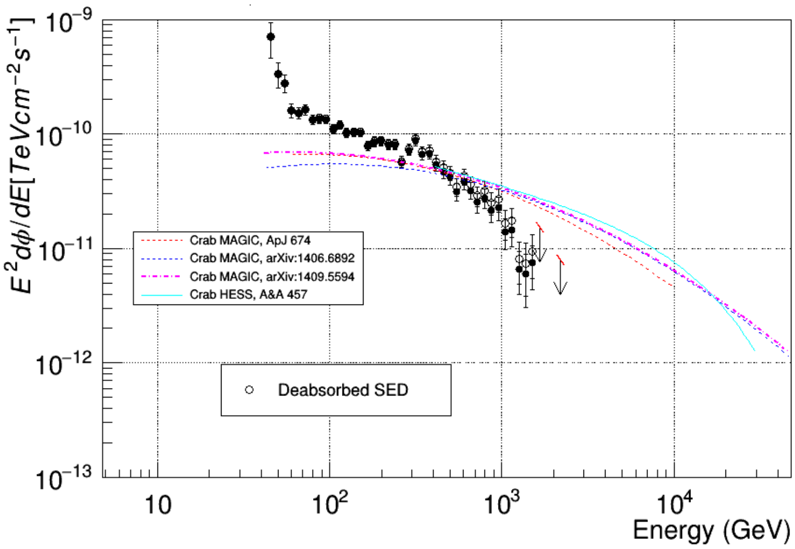

Figure 28: SED NGC 1275 during the flaring state, calculated by the program `Flute` (before unfolding procedure).

method	EPWL	ELP	LP	PWL
χ^2/ d.o.f.	18.1/11	18.1/10	35.7/11	78.5/12
Probability	0.1	0.1	2.0×10^{-4}	8.1×10^{-12}

Table 4: `Fold` fit models comparison.

collected during the same night. The SED of the flaring state is shown in Fig. 28. Using the executable `Fold` from `MARS`, four different functions are tested to fit the observed and intrinsic spectra respectively, and the resulting χ^2 values of those fits are reported in Tab. 4.

The best fit, out of 4 fits tried, turned out to be an EPWL. For the purposes of this thesis there is no need to search for a better fit. Reason for that is the fact that no perfect fit is searched here, but rather approximate fit that would allow to be "folded" with ALPs predictions and compared with intrinsic SED obtained with `Fold`. The EPWL function obtained by this fit is an approximated spectrum which is assumed to represent the SED without ALPs contributions. The convolution of the EPWL fit with $P_{\gamma\gamma}$ will represent the SED in presence of ALPs, and will be compared with the SED points and searched for matches and similarities. In this preliminary study the check will be performed by comparing the sums of squared residuals for each set and searching for the lowest value. More detailed comparison won't be performed, but in the near future a more precise test with a binned likelihood like it was done in [2] for *Fermi*-LAT data is planned. The red

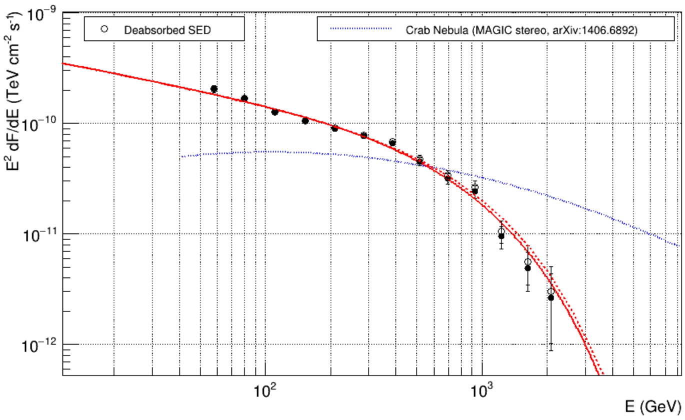

Figure 29: Unfolded SED of flaring state with EPWL fit.

line in Fig. 29 is representing EPWL fit and black dots are points of unfolded SED of NGC 1275 flaring state.

Furthermore, additional unfolding using `Combunfold` was done, using all the methods available. Results obtained using those methods are compared in Fig. 30.

From Fig. 30 one can see that the SED is stable under the unfolding with the different methods. The energy range in which those methods are compatible is the energy range 50 GeV - 700 GeV.

The final step is to calculate the sum of squared residuals between the points and convolutions in order to distinguish the most promising sets of ALPs parameters. For this calculation, Eq. 56. was used.

$$R_{\gamma ALPs} = \sum_{i=1}^{n} \left(\frac{f(x_i) - y_i}{\sigma_i} \right)^2, \tag{56}$$

where $f(x_i)$ are the values of the convolution evaluated in the bins i (from 1 to 39), y_i are the values of intrinsic SED, and σ_i are the SED statistical errors in each bin i. Final results of the residuals calculation are presented in Tab. 5.

For the final comparison, 10 different sets of m_a and g_{11} are chosen and the comparison between SED points and convolution of the $P_{\gamma\gamma}$ with the EPWL fit are shown in Fig. 31.

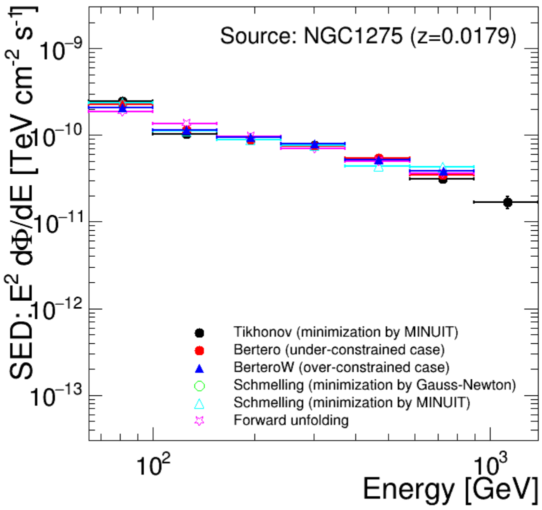

Figure 30: `Combunfold` methods comparison for flaring state of NGC 1275.

Set	m_a/neV	g_{11}	$R_{\gamma ALPs}$
S1	90	0.3	64.6
S2	90	0.5	79.9
S3	95	0.3	56.6
S4	95	0.5	76.1
S5	100	0.3	65.3
S6	100	0.5	67.4
S7	105	0.3	64.0
S8	105	0.5	70.7
S9	110	0.3	56.9
S10	110	0.5	55.3

Table 5: Values of sums of squared residuals for different sets of ALPs parameters in comparison to intrinsic SED of NGC1275.

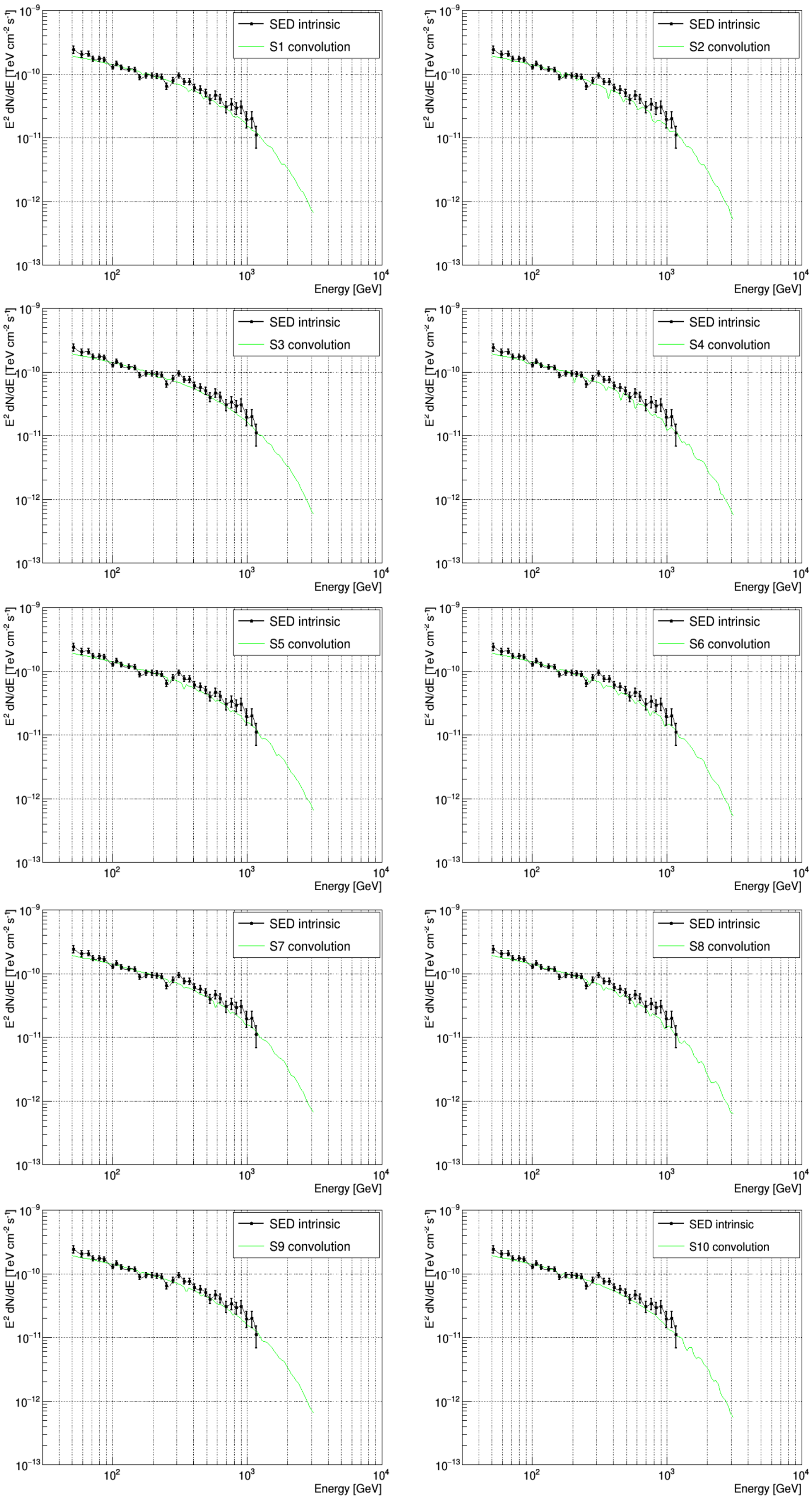

Figure 31: Comparison of SED points and convolution obtained using sets S1 to S10.

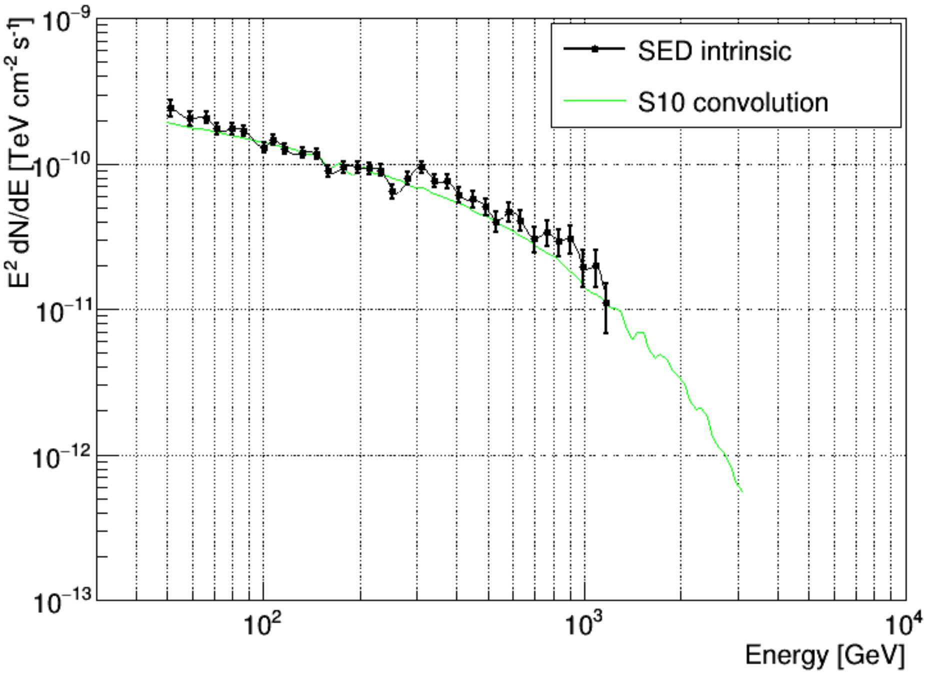

Figure 32: Comparison of intrinsic SED and convolution made with $m_a =$ 110 neV and $g_{11} = 0.5$ (S10).

From Tab. 5 it can be seen that the S10 set, corresponding to $m_a =$ 110 neV and coupling $g_{11} = 0.5$ (Fig. 32) has the lowest value of sum of squared residuals, which means that, among 10 sets of parameters studied here, is the most promising when compared with the intrinsic spectra obtained with MAGIC analysis.

6 Conclusions

In this work of thesis, the analysis of NGC 1275 was performed on MAGIC data collected during the ST_03_06 and ST_03_07 with 9.0 and 45.1 hours of data, respectively. The data were analyzed using the MAGIC software `MARS` available for MAGIC members. After the quality cuts applied and 8.3 hours of data for ST_03_06 and 43.3 hours of data ST_03_07 survived. Period ST_03_06 was excluded for having a total significance of the signal below 5 σ, and only ST_03_07 data was used for further analysis. After obtaining the light curve of the whole sample, three different states of the source were identified. Due to higher significances, higher signal to noise ratio, and higher statistics, it was decided to use the "flaring" state for applying the ALPs predictions. Also, the SED was unfolded and found stable in the 50 GeV - 700 GeV energy range.
A study on the ALPs parameter space was performed. The photon survival probability $P_{\gamma\gamma}$ was calculated by the GammaALPs code for several sets of parameters, among which, 10 were selected for the production of final plots. The obtained 10 $P_{\gamma\gamma}$ probabilities were folded with an EPWL function which was found as the most probable fit to the SED of the flaring state of the source. The convolution, performed by a python code, was then compared with the unfolded intrinsic SED of the flaring state of the source, in search of matches between the "wiggles". The comparison was performed calculating the sum of for the 10 sets studied. From the final results the favored values of the ALPs mass and coupling are 110 neV and 0.5, respectively, although additional calculations using a likelihood function are needed.
In order to have a deeper insight into this problem, additional studies on other sources are suggested. Future plans for this study include the creation of a list of candidates sources for the search of ALPs signatures in the spectrum of VHE γ-ray AGNs. The study here performed could be extended to the data collected by the new generation of VHE γ-ray detectors such as the (CTA) [23]. For CTA it is expected that the part of the ALPs parameter available for searching with γ-ray observations could be extended to higher masses of ALPs [68].

References

[1] Peccei, R.D. and Quinn, H.R. CP conservation in the presence of pseudoparticles. *Phys. Rev. Lett.*, 38:1440–1443, Jun 1977. doi: 10.1103/PhysRevLett.38.1440. URL `https://link.aps.org/doi/10.1103/PhysRevLett.38.1440`.

[2] Ajello, M. et al. Search for Spectral Irregularities due to Photon-Axionlike-Particle Oscillations with the Fermi Large Area Telescope. , 116(16):161101, April 2016. doi: 10.1103/PhysRevLett.116.161101.

[3] Du, N. et al. Search for invisible axion dark matter with the axion dark matter experiment. *Phys. Rev. Lett.*, 120:151301, Apr 2018. doi: 10.1103/PhysRevLett.120.151301. URL `https://link.aps.org/doi/10.1103/PhysRevLett.120.151301`.

[4] collaboration V. Anastassopoulos, C. et al. New cast limit on the axion-photon interaction. *Nature Physics*, 13:584–590, 2017.

[5] Sanchez-conde, M. et al. Hints of the existence of axion-like-particles from the gamma-ray spectra of cosmological sources. 2009.

[6] Abbott, L. and Sikivie, P. A cosmological bound on the invisible axion. *Physics Letters B*, 120(1):133 – 136, 1983. ISSN 0370-2693. doi: https://doi.org/10.1016/0370-2693(83)90638-X. URL `http://www.sciencedirect.com/science/article/pii/037026938390638X`.

[7] Meyer, M., Horns, D. and Raue, M. First lower limits on the photon-axion-like particle coupling from very high energy gamma-ray observations. *Phys. Rev. D*, 87(3):035027, 2013. doi: 10.1103/PhysRevD.87.035027.

[8] Malyshev, D.V. et al. Improved limit on axion-like particles from gamma-ray data on perseus cluster. *arXiv: High Energy Astrophysical Phenomena*, 2018.

[9] Aharonian, F. et al. High energy astrophysics with ground-based gamma ray detectors. *Reports on Progress in Physics*, 71(9):096901, September 2008. doi: 10.1088/0034-4885/71/9/096901.

[10] Peccei, R.D. *The Strong CP Problem and Axions*, volume 741, page 3. 2008.

[11] Weinberg, S. The u(1) problem. *Phys. Rev. D*, 11:3583–3593, Jun 1975. doi: 10.1103/PhysRevD.11.3583. URL `https://link.aps.org/doi/10.1103/PhysRevD.11.3583`.

[12] 't Hooft, G. Symmetry breaking through bell-jackiw anomalies. *Phys. Rev. Lett.*, 37:8–11, Jul 1976. doi: 10.1103/PhysRevLett.37.8. URL `https://link.aps.org/doi/10.1103/PhysRevLett.37.8`.

[13] 't Hooft, G. Computation of the quantum effects due to a four-dimensional pseudoparticle. *Phys. Rev. D*, 14:3432–3450, Dec 1976. doi: 10.1103/PhysRevD.14.3432. URL `https://link.aps.org/doi/10.1103/PhysRevD.14.3432`.

[14] Adler, S.L. Axial-vector vertex in spinor electrodynamics. *Phys. Rev.*, 177:2426–2438, Jan 1969. doi: 10.1103/PhysRev.177.2426. URL `https://link.aps.org/doi/10.1103/PhysRev.177.2426`.

[15] Abel, C. et al. Measurement of the Permanent Electric Dipole Moment of the Neutron. , 124(8):081803, February 2020. doi: 10.1103/PhysRevLett.124.081803.

[16] Peccei, R.D. and Quinn, H.R. Constraints imposed by CP conservation in the presence of pseudoparticles. *Phys. Rev. D*, 16:1791–1797, Sep 1977. doi: 10.1103/PhysRevD.16.1791. URL `https://link.aps.org/doi/10.1103/PhysRevD.16.1791`.

[17] Weinberg, S. A new light boson? *Phys. Rev. Lett.*, 40:223–226, Jan 1978. doi: 10.1103/PhysRevLett.40.223. URL `https://link.aps.org/doi/10.1103/PhysRevLett.40.223`.

[18] Wilczek, F. Problem of strong p and t invariance in the presence of instantons. *Phys. Rev. Lett.*, 40:279–282, Jan 1978. doi: 10.1103/PhysRevLett.40.279. URL `https://link.aps.org/doi/10.1103/PhysRevLett.40.279`.

[19] Graham, P.W. et al. Experimental searches for the axion and axion-like particles. *Annual Review of Nuclear and Particle Science*, 65:485–514, 2015.

[20] Sulc, M. et al. Axion search by laser-based experiment OSQAR. *Nucl. Instrum. Meth. A*, 718:530–532, 2013. doi: 10.1016/j.nima.2012.11.107.

[21] Sikivie, P. Experimental tests of the "invisible" axion. *Phys. Rev. Lett.*, 51:1415–1417, Oct 1983. doi: 10.1103/PhysRevLett.51.1415. URL `https://link.aps.org/doi/10.1103/PhysRevLett.51.1415`.

[22] Arias, P.A. et al. Wispy cold dark matter. *Journal of Cosmology and Astroparticle Physics*, 2012:013–013, 2012.

[23] Consortium, T.C. Design concepts for the cherenkov telescope array. 2010.

[24] de Angelis, A.D. et al. Photon propagation and the very high energy -ray spectra of blazars: how transparent is the universe? *Monthly Notices of the Royal Astronomical Society: Letters*, 394, 2008.

[25] Horns, D. and Meyer, M. Indications for a pair-production anomaly from the propagation of vhe gamma-rays. *Journal of Cosmology and Astroparticle Physics*, 2012:033–033, 2012.

[26] Troitsky, S.V. Axion-like particles and the propagation of gamma rays over astronomical distances. *JETP Letters*, 105:55–59, 2017.

[27] Domínguez, A. et al. Extragalactic background light inferred from AEGIS galaxy-SED-type fractions. , 410(4):2556–2578, Feb 2011. doi: 10.1111/j.1365-2966.2010.17631.x.

[28] Hooper, D. and Serpico, P.D. Detecting axionlike particles with gamma ray telescopes. *Physical review letters*, 99 23:231102, 2007.

[29] Hochmuth, K.A. and Sigl, G. Effects of axion-photon mixing on gamma-ray spectra from magnetized astrophysical sources. 2007.

[30] Bassan, N. and Roncadelli, M. Photon-axion conversion in active galactic nuclei? 2009.

[31] de Angelis, A.D., Roncadelli, M. and Mansutti, O. Evidence for a new light spin-zero boson from cosmological gamma-ray propagation? 2007.

[32] Horns, D. et al. Hardening of tev gamma spectrum of agns in galaxy clusters by conversions of photons into axion-like particles. *Physical Review D*, 86:075024, 2012.

[33] collaboration, H. H.e.s.s. first public test data release. 2018.

[34] T.C.Weekes and et al. Veritas: the very energetic radiation imaging telescope array system. 2001.

[35] Weekes, T.C. et al. Observation of TeV Gamma Rays from the Crab Nebula Using the Atmospheric Cerenkov Imaging Technique. , 342:379, July 1989. doi: 10.1086/167599.

[36] Acharya, T.C.T.A.C.B. et al. Science with the cherenkov telescope array. *International Journal of Modern Physics D*, 2015.

[37] Čerenkov, P.A. Visible Radiation Produced by Electrons Moving in a Medium with Velocities Exceeding that of Light. *Physical Review*, 52 (4):378–379, August 1937. doi: 10.1103/PhysRev.52.378.

[38] Jelley, J.V. *Cherenkov Radiation: Its Properties, Occurrence, and Uses*, pages 275–318. Springer US, Boston, MA, 1983. ISBN 978-1-4684-4505-3. doi: 10.1007/978-1-4684-4505-3_6. URL https://doi.org/10.1007/978-1-4684-4505-3_6.

[39] Frank, I. and Tamm, I. Coherent visible radiation of fast electrons passing through matter. *Compt. Rend. Acad. Sci. URSS*, 14(3):109–114, 1937. doi: 10.3367/UFNr.0093.196710o.0388.

[40] Watson, A.A. The discovery of cherenkov radiation and its use in the detection of extensive air showers. *Nuclear Physics B - Proceedings Supplements*, 212-213:13 – 19, 2011. ISSN 0920-5632. doi: https://doi.org/10.1016/j.nuclphysbps.2011.03.003. URL http://www.sciencedirect.com/science/article/pii/S0920563211000363. Proceedings of the Cosmic Ray International Seminars (CRIS 2010).

[41] Jelley, J.V. and Porter, N.A. Cerenkov Radiation from the Night Sky. , 4:275, March 1963.

[42] Hillas, A.M. Cerenkov Light Images of EAS Produced by Primary Gamma Rays and by Nuclei. In *19th International Cosmic Ray Conference (ICRC19), Volume 3*, volume 3 of *International Cosmic Ray Conference*, page 445, August 1985.

[43] De Angelis, A. and Pimenta, M. *Introduction to Particle and Astroparticle Physics.* 2018. doi: 10.1007/978-3-319-78181-5.

[44] Blandford, R., Meier, D. and Readhead, A.C.S. Relativistic jets in active galactic nuclei. *arXiv: High Energy Astrophysical Phenomena*, 2018.

[45] Spurio, M. *Particles and Astrophysics.* 11 2014. doi: 10.1007/978-3-319-08051-2.

[46] Konopelko, A. et al. Modeling the TeV gamma-ray spectra of two low-redshift active galactic nuclei: Markarian 501 and markarian 421. *The Astrophysical Journal*, 597(2):851–859, nov 2003. doi: 10.1086/374593. URL https://doi.org/10.1086%2F374593.

[47] Vermeulen, R.C., Readhead, A.C.S. and Backer, D.C. Discovery of a Nuclear Counterjet in NGC 1275: A New Way to Probe the Parsec-Scale Environment. , 430:L41, July 1994. doi: 10.1086/187433.

[48] Abdo, A.A. et al. FERMIDISCOVERY OF GAMMA-RAY EMISSION FROM NGC 1275. *The Astrophysical Journal*, 699(1):31–39, jun 2009. doi: 10.1088/0004-637x/699/1/31. URL `https://doi.org/10.1088%2F0004-637x%2F699%2F1%2F31`.

[49] Aleksi'c, M.C.J. et al. Detection of very high energy gamma-ray emission from ngc 1275 by the magic telescopes. *Astronomy and Astrophysics*, 539, 2012.

[50] collaboration V. A. Acciari, M. et al. Constraining dark matter lifetime with a deep gamma-ray survey of the perseus galaxy cluster with magic. *Physics of the Dark Universe*, 22:38–47, 2018.

[51] Aleksi'c, M.C.J. et al. Constraining cosmic rays and magnetic fields in the perseus galaxy cluster with tev observations by the magic telescopes. *Astronomy and Astrophysics*, 541, 2012.

[52] Aleksić, J. et al. The major upgrade of the MAGIC telescopes, Part I: The hardware improvements and the commissioning of the system. *Astroparticle Physics*, 72:61–75, January 2016. doi: 10.1016/j.astropartphys.2015.04.004.

[53] Aleksić, J. et al. The major upgrade of the MAGIC telescopes, Part II: A performance study using observations of the Crab Nebula. *Astroparticle Physics*, 72:76–94, January 2016. doi: 10.1016/j.astropartphys.2015.02.005.

[54] Ansoldi, M.C.S. et al. Gamma-ray flaring activity of ngc1275 in 2016–2017 measured by magic. *Astronomy and Astrophysics*, 617:91, 2018.

[55] Albert, J. et al. Implementation of the random forest method for the imaging atmospheric cherenkov telescope magic. *Nuclear Instruments and Methods in Physics Research Section A: Accelerators, Spectrometers, Detectors and Associated Equipment*, 588(3):424–432, Apr 2008. ISSN 0168-9002. doi: 10.1016/j.nima.2007.11.068. URL `http://dx.doi.org/10.1016/j.nima.2007.11.068`.

[56] Li, T.P. and Ma, Y.Q. Analysis methods for results in gamma-ray astronomy. , 272:317–324, September 1983. doi: 10.1086/161295.

[57] Raffelt, G. and Stodolsky, L. Mixing of the photon with low-mass particles. *Phys. Rev. D*, 37:1237–1249, Mar 1988. doi: 10.1103/PhysRevD.37.1237. URL `https://link.aps.org/doi/10.1103/PhysRevD.37.1237`.

[58] Mirizzi, A. and Montanino, D. Stochastic conversions of tev photons into axion-like particles in extragalactic magnetic fields. *Journal of Cosmology and Astroparticle Physics*, 2009(12):004–004, Jan 2017. ISSN 1475-7516. doi: 10.1088/1475-7516/2009/12/004. URL `http://dx.doi.org/10.1088/1475-7516/2009/12/004`.

[59] Sánchez-Conde, M.A. et al. Hints of the existence of axionlike particles from the gamma-ray spectra of cosmological sources. *Physical Review D*, 79(12), Jun 2009. ISSN 1550-2368. doi: 10.1103/physrevd.79.123511. URL `http://dx.doi.org/10.1103/PhysRevD.79.123511`.

[60] Meyer, M. *The Opacity of the Universe for High and Very High Energy γ-Rays*. PhD thesis, Hamburg U., 2013.

[61] Mirizzi, A., Raffelt, G.G. and Serpico, P.D. Photon-axion conversion in intergalactic magnetic fields and cosmological consequences. *Axions*, page 115–134. doi: 10.1007/978-3-540-73518-2_7. URL `http://dx.doi.org/10.1007/978-3-540-73518-2_7`.

[62] Ayala, A. et al. Revisiting the bound on axion-photon coupling from globular clusters. *Physical Review Letters*, 113(19), Nov 2014. ISSN 1079-7114. doi: 10.1103/physrevlett.113.191302. URL `http://dx.doi.org/10.1103/PhysRevLett.113.191302`.

[63] Payez, A. et al. Revisiting the sn1987a gamma-ray limit on ultralight axion-like particles. *Journal of Cosmology and Astroparticle Physics*, 2015:006–006, 2015.

[64] Meyer, M., Montanino, D. and Conrad, J. On detecting oscillations of gamma rays into axion-like particles in turbulent and coherent magnetic fields. *Journal of Cosmology and Astroparticle Physics*, 2014(09):003–003, Jan 2017. ISSN 1475-7516. doi: 10.1088/1475-7516/2014/09/003. URL `http://dx.doi.org/10.1088/1475-7516/2014/09/003`.

[65] Churazov, E. et al. Xmm-newtonobservations of the perseus cluster. i. the temperature and surface brightness structure. *The Astrophysical Journal*, 590(1):225–237, Jun 2003. ISSN 1538-4357. doi: 10.1086/374923. URL `http://dx.doi.org/10.1086/374923`.

[66] Vacca, V. et al. The intracluster magnetic field power spectrum in a2199. *Astronomy and Astrophysics*, 540, 2012.

[67] Jansson, R. and Farrar, G.R. A new model of the galactic magnetic field. *The Astrophysical Journal*, 757(1):14, Aug 2012. ISSN 1538-4357. doi: 10.1088/0004-637x/757/1/14. URL `http://dx.doi.org/10.1088/0004-637X/757/1/14`.

[68] Actis, M. et al. Design concepts for the Cherenkov Telescope Array CTA: an advanced facility for ground-based high-energy gamma-ray astronomy. *Experimental Astronomy*, 32(3):193–316, December 2011. doi: 10.1007/s10686-011-9247-0.